



High-resolution UV/Optical/IR Imaging of Jupiter in 2016–2019

Michael H. Wong¹ , Amy A. Simon² , Joshua W. Tollefson^{1,3} , Imke de Pater^{1,3} , Megan N. Barnett⁴ , Andrew I. Hsu³ , Andrew W. Stephens⁵ , Glenn S. Orton⁶ , Scott W. Fleming⁷ , Charles Goullaud³, William Januszewski⁷ , Anthony Roman⁷ , Gordon L. Bjoraker⁸ , Sushil K. Atreya⁹, Alberto Adriani¹⁰ , and Leigh N. Fletcher¹¹

¹ Center for Integrative Planetary Science, University of California, Berkeley, CA 94720, USA

² Solar System Exploration Division, NASA Goddard Space Flight Center, Greenbelt, MD 20771, USA

³ Astronomy Department, University of California, Berkeley, CA 94720, USA

⁴ Department of Geophysical Sciences, University of Chicago, Chicago, IL 60637, USA

⁵ Gemini Observatory North, NSF's National Optical-Infrared Astronomy Research Laboratory, Hilo, HI 96720, USA

⁶ NASA Jet Propulsion Laboratory, California Institute of Technology, Pasadena, CA 91109, USA

⁷ Space Telescope Science Institute, Baltimore, MD 21218, USA

⁸ Code 693, NASA Goddard Space Flight Center, Greenbelt, MD 20771, USA

⁹ Department of Climate and Space Sciences and Engineering, University of Michigan, Ann Arbor, MI 48109, USA

¹⁰ INAF—Istituto di Astrofisica e Planetologia Spaziali, 00133 Roma, Italy

¹¹ School of Physics and Astronomy, University of Leicester, Leicester LE1 7RH, UK

Received 2019 August 31; revised 2020 February 6; accepted 2020 February 8; published 2020 April 1

Abstract

Imaging observations of Jupiter with high spatial resolution were acquired beginning in 2016, with a cadence of 53 days to coincide with atmospheric observations of the Juno spacecraft during each perijove pass. The Wide Field Camera 3 (WFC3) aboard the Hubble Space Telescope (HST) collected Jupiter images from 236 to 925 nm in 14 filters. The Near-Infrared Imager (NIRI) at Gemini North imaged Jovian thermal emission using a lucky-imaging approach (co-adding the sharpest frames taken from a sequence of short exposures), using the M' filter at 4.7 μm . We discuss the data acquisition and processing and an archive collection that contains the processed WFC3 and NIRI data (doi:10.17909/T94T1H). Zonal winds remain steady over time at most latitudes, but significant evolution of the wind profile near 24°N in 2016 and near 15°S in 2017 was linked with convective superstorm eruptions. Persistent mesoscale waves were seen throughout the 2016–2019 period. We link groups of lightning flashes observed by the Juno team with water clouds in a large convective plume near 15°S and in cyclones near 35°N–55°N. Thermal infrared maps at the 10.8 micron wavelength obtained at the Very Large Telescope show consistent high brightness temperature anomalies, despite a diversity of aerosol properties seen in the HST data. Both WFC3 and NIRI imaging reveal depleted aerosols consistent with downwelling around the periphery of the 15°S storm, which was also observed by the Atacama Large Millimeter/submillimeter Array. NIRI imaging of the Great Red Spot shows that locally reduced cloud opacity is responsible for dark features within the vortex. The HST data maps multiple concentric polar hoods of high-latitude hazes.

Unified Astronomy Thesaurus concepts: Jupiter (873); Planetary atmospheres (1244); Time series analysis (1916); Direct imaging (387); Seasonal phenomena (1437); Astrophysical fluid dynamics (101); Hubble Space Telescope (761); Ground-based astronomy (686); Atmospheric variability (2119); Clouds (258)

1. Introduction

The era of high-resolution Jupiter imaging at visible wavelengths began in space, with the Pioneer and Voyager spacecraft flybys (Fountain et al. 1974; Smith et al. 1979). These missions gave the first looks at discrete features like convective plumes and the first accurate measurements of the zonal winds (or differential rotation). The Hubble Space Telescope (HST) has continued to image the planet at high resolution, as have the Galileo and Juno missions to Jupiter, and flybys from missions like Cassini and New Horizons. Although velocities have been measured in specific locations using Galileo and New Horizons data (Gierasch et al. 2000; Hueso et al. 2009), only Voyager, HST, and Cassini have done significant time-series imaging capable of measuring the dynamics of jets, waves, and vortices on a global scale (Limaye 1986; Simon-Miller et al. 2012). Both manual tracking (Mitchell et al. 1981) and automated correlation

(e.g., Choi et al. 2007; Asay-Davis et al. 2009) methods have been used to measure velocities from image sequences.

At longer wavelengths near 5 μm , Jupiter has weak molecular absorption and, thus, emits thermal radiation from deeper levels of 4–7 bar (Bjoraker et al. 1986). Like a jack-o'-lantern, Jupiter's appearance is marked by bright “hot spots” that are free from overlying cloud opacity. The inhomogeneous pattern of 5 μm emission is primarily observed from ground-based facilities (Westphal 1969; Harrington et al. 1996; Ortiz et al. 1998), since the terrestrial atmosphere has good transparency in the infrared M -band (Tokunaga 2000), and large telescopes can provide images with excellent angular resolution, particularly when improved with an adaptive optics approach (de Pater et al. 2010, 2011) or a lucky-imaging approach (Fletcher et al. 2018), where many short exposures are taken and the sharpest frames are co-added. NASA's giant planet flagship orbiters, Galileo and Cassini, carried imaging spectrometers that covered the 5 μm range (Carlson et al. 1992; Miller et al. 1996), and Juno's JIRAM instrument has produced low-resolution spectra and stunning images of Jupiter's atmosphere, particularly in polar regions (Sindoni et al. 2017; Adriani et al. 2018b).



Original content from this work may be used under the terms of the [Creative Commons Attribution 4.0 licence](https://creativecommons.org/licenses/by/4.0/). Any further distribution of this work must maintain attribution to the author(s) and the title of the work, journal citation and DOI.

Table 1
WFC3/UVIS Filters Used in Relevant Jupiter Programs

Filter	t_{exp} (s) ^a	S/N ^b	Programs ^c	Objectives
F225W	40	85	WFCJ, VLA	Haze structure/distribution
F275W	20	125	WFCJ, OPAL, VLA	Haze structure/distribution
F343N	6	160	WFCJ, OPAL, VLA	Haze distribution/composition
F395N	9	155	WFCJ, OPAL, VLA	Haze distribution/composition
F467M	1.2	170	OPAL	Haze distribution/composition
F502N	4	170	WFCJ, OPAL, VLA	Haze distribution/composition
F547M	0.48	200	OPAL	Haze distribution/composition
F631N	4	175	WFCJ, OPAL, VLA	Velocities, cloud structure/distribution
F658N	8	170	OPAL	Cloud distribution/composition
FQ727N	8	150	WFCJ, VLA	Cloud structure/distribution
FQ750N	6	180	WFCJ, VLA	Cloud structure/distribution
FQ889N	15, 53	70, 130	WFCJ, OPAL, VLA	Cloud/haze structure/distribution
FQ906N ^d	15	170	WFCJ	Cloud structure/distribution
FQ924N ^d	12	170	WFCJ	Cloud structure/distribution

Notes.

^a Exposure times listed are typical/recommended values. Actual exposure times vary from frame to frame for some filters, as necessary to schedule observations within limited HST visibility windows. For WFCJ, some HST orbits have filters omitted for scheduling reasons.

^b S/N is the mean signal-to-noise ratio from Poisson-distributed detector noise in a single pixel of a single image.

^c WFCJ programs include GO-14661 and GO-15159. HST programs in support of VLA observations are GO-14839, GO-14936, and GO-15665. OPAL programs for 2016–2019 are GO-14334, GO-14756, GO-15262, and GO-15502, respectively.

^d Filters FQ906N and FQ924N were used only for PJ15 observations, because scheduling reasons (lack of guide stars) prevented use of FQ889N at that time.

During each spacecraft pass, Juno dips down to 3400–8000 km above the cloud tops at closest approach, and these “perijove” (or PJ) encounters occur once every 53 days in Juno’s highly eccentric ($e = 0.98$) orbit (Bolton et al. 2017). Juno’s MWR instrument (Janssen et al. 2017) has produced remarkable new observations of ammonia opacity and lightning sferics during perijove passes (Li et al. 2017; Brown et al. 2018). Like cloud opacity, both ammonia mixing ratio (Gierasch et al. 1986; Achterberg et al. 2006) and lightning flashes are tracers of dynamics: upwelling air tends to have more cloud condensation, higher volatile mixing ratios, and even lightning in the case of moist convection. Downwelling air tends to be depleted in condensable volatiles relative to the surroundings, and depleted in cloud opacity as well.

This paper reports on a sequence of high-resolution imaging data, covering the 250–900 nm range with multiple HST/UVIS filters and the 4.7 μm wavelength with Gemini/Near-Infrared Imager (NIRI). The core motivation of the data set is to provide consistent context imaging for Juno passes. Some early elements of the data set depart from the regular 53 day cadence because some ground-based observations could not be re-planned to adjust to changes in the Juno trajectory plan (Bolton et al. 2017). This paper provides a complete description of the data set, which is available in raw and processed forms online, in order to facilitate future research. Sections 2 and 3 describe the acquisition and processing of the HST and Gemini components of the data set, Section 4 describes the high-level science products (HLSPs) produced from the observations and available online, and Section 5 gives an overview of science results to date. This paper covers data collected in the 2016–2019 time period. More observations are planned and/or proposed for future dates throughout the remainder of the Juno mission.

2. HST WFC3 Imaging Data

We use the UVIS channel of the WFC3 instrument to obtain high-resolution imaging of Jupiter in the UV–NIR range. A

description of the instrument, including filter central wavelengths and bandpasses, is given by Dressel (2019). Filters used for the Jupiter observations reported here are listed in Table 1. Several specific observing modes, settings, and best practices are commonly used for Jupiter and other planetary observations. Details of these settings have been omitted from prior publications, but we describe them in Sections 2.1–2.7 for completeness, for potential benefit to other observers, and to ensure that data products in the MAST archive (Section 4) are fully described. Readers who are uninterested in the details of planning HST observations might skip to Section 2.8, which discusses the temporal sampling within the data set.

2.1. Quad Filters

In WFC3, a range of methane-band filters are included as “quad” spectral elements, such that each one of them covers a quadrant of the overall WFC3/UVIS detector. Methane-band filters are centered on CH_4 gas absorption bands at 619, 727, and 889 nm. Within methane bands, light is only scattered back from high-altitude clouds, while images in continuum filters are unaffected by methane absorption and can, thus, detect deeper clouds. Additional narrowband filters were included in the WFC3 design with central wavelengths stepping along the edge of the strong methane band at 889 nm, specifically for the purpose of solar system and brown dwarf atmospheric studies (see Lupie et al. 2000). The availability of so many narrowband spectral elements is particularly beneficial for studies of aerosol vertical profiles (Table 1), but special care must be taken with target placement due to the quad nature of these filters.

Two constraints apply to target placement when using the quad filters: filter edge effects and guide star tracking. Near the inner boundaries of the quad filters lies a plus-shaped region (Figure 1) where data cannot be photometrically calibrated because the defocused, adjacent filters contribute light with blended spectral contributions. In normal use of these filters (i.e., positioning the target at the default reference point for

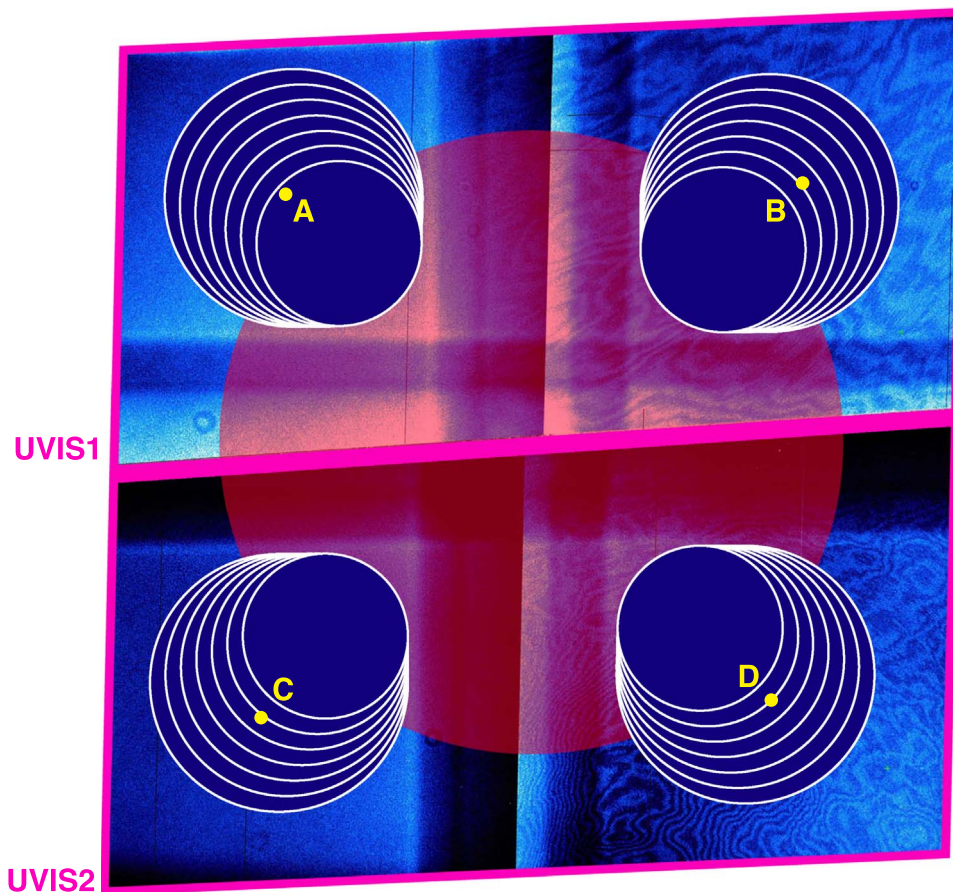


Figure 1. Targets in quad-filter exposures need to be carefully placed on the WFC3/UVIS detector in order to stay clear of filter edge effects (large central plus-shaped pattern in the blue background) but to keep slews inside a $120''$ diameter region (large red central circle). If exceeded, the $120''$ slew limit would trigger a new guide star acquisition (requiring 6 min overhead). The exact position adjustment depends on the size of the target (nested circles have diameters of $32''$ – $50''$). Reference points for each quadrant are labeled in yellow; Table 2 gives linear coefficients for offsets with respect to these reference points as a function of quadrant and target size. The figure is rectilinear in the sky coordinate frame, so the envelope of the UVIS detector forms a rhombus shape due to the tilt of the focal plane with respect to the optical axis.

quad subarrays, Section 6.4.5 of Dressel 2019), the target lies in the center of the area unaffected by the filter edges, and filter edge effects are minimized. We deviate slightly from this normal use in order to maximize guide star availability.

Guide star availability becomes an issue when multiple quad filters are used, because any slew of $2'$ or more requires new guide stars to be acquired. The time needed to re-acquire guide stars reduces the amount of science time available in an orbit by about 8 minutes. Slewing between quad-filter reference points (yellow points in Figure 1) can easily exceed the $2'$ limit for using the same guide stars (red circle in Figure 1). Several programs use FQ727N, FQ750N, and FQ889N, which requires slewing the target to place it on quadrants D, B, and A, respectively (Table 2). In many cases, the target is also placed in quadrant C in order to use the subarrays defined there, thus introducing slews between all four quadrants. Balancing these two constraints (quadrant usage versus slew size) is improved by adjusting the target position with respect to the default reference positions for each quad aperture.

These position adjustments (called POS TARG in the HST planning system) were crudely estimated prior to 2018 July. In observations from 2018 July and later, we use simple linear expressions to determine POS TARG values, as a function of quadrant and target radius. Coefficients m and b in the relation $\text{POS TARG} = mD + b$, where D is the target diameter in

Table 2
Coefficients for Target Offsets^a in WFC3/UVIS Quad-filter Exposures

Quadrant	Relevant Filters	POS TARG X		POS TARG Y	
		m^b	b''	m	b''
A	FQ889N	-0.450	+23.07	+0.527	-27.24
B	FQ750N	+0.537	-34.46	+0.465	-26.79
C	FQ906N	-0.531	+29.68	-0.468	+30.19
D	FQ727N, FQ924N	+0.453	-28.25	-0.532	+32.22

Notes.

^a POS TARG offsets are designed to minimize HST slews between WFC3/UVIS quadrants (see Figure 1). These offsets are ideal for circular targets of any apparent diameter D (in arcseconds). Offsets are defined for UVIS-QUAD-SUB reference pixel aperture positions (yellow dots in Figure 1) in use at the time of publication: A (796, 1306), B (3330, 1226), C (787, 816), and D (3294, 766).

^b Coefficients give POS TARG values as a function of diameter D : $\text{POS TARG} = mD + b$.

arcseconds, are given in Table 2. For example, when Jupiter's diameter is $38''$, POS TARG X,Y values for quad A (e.g., FQ889N) would be $+5''.99$, $-7''.24$. These relations minimize slews while avoiding filter edge effects for any circular target of Jupiter size or smaller.

2.2. Fringing

Fringing is a source of photometric error and large-scale pattern noise that affects narrowband filters at wavelengths >650 nm (Wong 2010). At long wavelengths, silicon becomes increasingly transparent, leading to constructive and destructive interference as incoming light experiences multiple internal reflections within the detector. The fringing amplitude has a strong dependence on the spectral energy distribution of the source convolved with the telescope throughput, and the pattern results from small variations in thickness across the detector. In Figure 1, the fingerprint-like fringing pattern is stronger in quads B and D (750 and 727 nm) than in quads A and C (619 and 634 nm), due to silicon’s transparency.

All long-wavelength narrowband WFC3 HLSPs described in Section 4, as well as all long-wavelength narrowband OPAL maps described in Simon et al. (2015), have been corrected for fringing using preliminary “fringe flatfields” as described in Wong (2011). These assume a Jupiter spectral energy distribution based on the disk-averaged reflectance spectrum of Jupiter (Karkoschka 1998) convolved with the solar spectrum (Colina et al. 1996). The correction is not perfect, but some options for future improvements have been identified. The WFC3/UVIS detector thickness solution derived from monochromatic calibration images is inconsistent between the two main calibration image data sets (Wong 2011). This inconsistency may be ameliorated by applying a correction for the “flare” window ghost effect, as has now been done for WFC3/UVIS pipeline flatfields (Mack et al. 2016). Improvements to the optical-wavelength spectrum of Jupiter, particularly as it varies across the disk, may be expected from new hyperspectral observations (Dahl et al. 2018; Braude et al. 2020).

2.3. Geometric Distortion

Geometric distortion in raw WFC3 images is primarily caused by the tilt between the telescope beam and the detector plane. The coordinate transformation correcting for distortion is applied by the *astrodrizzle* task, which calls several reference files to determine the appropriate corrections. The *astrodrizzle* task is distributed within the AstroConda¹² package of analysis software currently supported by STScI. Polynomial and lookup-table corrections are provided by the IDCTAB and NPOLFILE reference files, respectively. Images are transformed from detector coordinates to sky coordinates in this *astrodrizzle* processing step.

Cosmic rays (and other transient nonideal pixel responses) affect many of the exposures. Frames with long exposure times are particularly susceptible to cosmic ray hits. Standard HST image processing is able to remove cosmic rays at the *astrodrizzle* step, by combining multiple images of fixed targets and by identifying cosmic rays as transient features. This approach cannot be used for image sequences of rotating bodies, especially when atmospheric change ensures that no two exposures are ever identical. Instead, we use the sharpness of the cosmic ray strikes themselves to clean them from single images, with the Laplacian edge-detection approach of van Dokkum (2001). Because the *astrodrizzle* distortion correction tends to blur the sharp edges of cosmic ray strikes, we must perform the single-image cosmic ray rejection procedure on UVIS data before correcting for distortion and transforming from detector coordinates to sky coordinates.

Distortion corrections differ slightly from filter to filter. Filter-dependent distortion solutions were used for the medium- and wide-band filters: filters ending with M or W in Table 1. For the narrowband filters, the best available distortion solution was the one derived from the F606W filter (Kozhurina-Platais 2014). Images were processed with this distortion solution, and maps and other High Level Science Products (Section 4) were produced and uploaded to the MAST archive.

Data taken after 2018 June benefit from new filter-specific distortion solutions for narrowband filters (those ending with N in Table 1, excepting the quad filters). These new solutions (Martlin et al. 2018) were used for data products based on exposures acquired after 2018 June. Comparison of maps made with the old (F606W) and new (narrowband filter-specific) distortion solutions suggest residual distortions slightly smaller than our navigation uncertainty, which is about $0^{\circ}.1$ of latitude/longitude at disk center. In the F631N filter, which we use for velocity retrievals, we found virtually no difference from using the newer corrections.

2.4. Shutter-induced Vibration

Planetary targets can be bright, and often require short exposure times (Table 1). For short WFC3/UVIS exposures, vibration from the shutter mechanism can degrade the image sharpness (Section 6.11.4 of Dressel 2019). For exposures shorter than 9 s, we specified the “A” side of the shutter blade, to minimize this effect. But in order to maximize the lifetime of WFC3/UVIS, operations are being changed as of mid-2019 to minimize mechanical movements caused when observers specify the A side of the shutter blade. Exposures longer than 5 s are deemed to be more strongly affected by focus changes due to breathing than by shutter-induced vibration.

2.5. Charge-transfer Efficiency

Charge-transfer efficiency (CTE) refers to the process of reading out the charge-coupled device (CCD) along parallel detector columns. As CCD detectors age (particularly in the harsh radiation environment of space), increasing numbers of photoelectrons become smeared out along the readout direction during detector readout, trailing behind the pixel where they were originally created. The HST observation planning tool (APT) generates warnings for observations that do not attempt to mitigate this issue (by flashing the detector with an internal LED lamp at the end of a science exposure). This post-flash operation evenly illuminates the whole detector, filling many charge traps and reducing inefficiency in the charge transfer.

We found that observations of bright extended targets do not require post-flash illumination, because the target effectively flashes the charge traps automatically. A substantial signal is carried in the extended wings of the point-spread function, so extended targets are surrounded by large halos. The halo is faint compared to the target itself, but it provides enough photons to fill charge traps in advance of any on-target pixels in the readout direction. Analysis of Uranus data (P. Fry 2015, private communication) showed that even the much fainter target suffered no astrometric error due to CTE effects.

Figure 2 shows the difference between uncorrected data (FLT files) and data with the pixel-based correction for CTE applied (FLC files; Baggett et al. 2015; Ryan et al. 2016). Comparing these two data products suggests that photometry on the planet’s disk differs by 0.25% or less due to CTE effects

¹² AstroConda documentation (at the time of writing) is available at <http://astroconda.readthedocs.io/>.

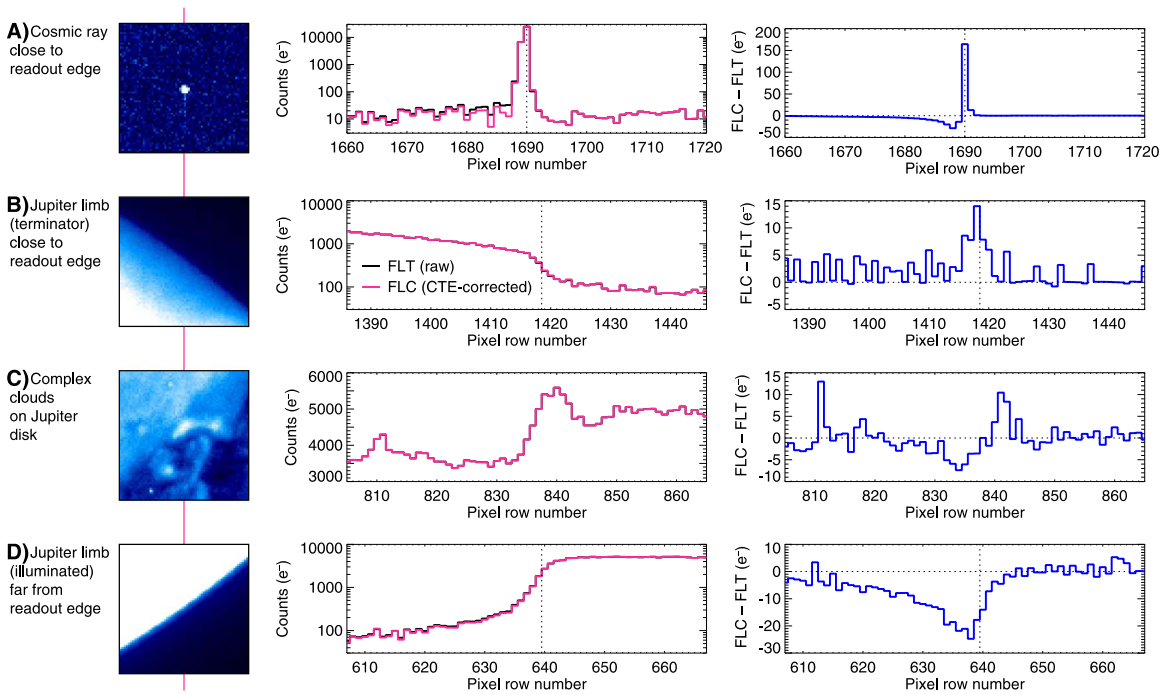


Figure 2. Charge-transfer efficiency has a minimal effect on photometry and astrometry for bright, extended sources like Jupiter. Each row shows a different detail of an HST image. The pink line behind the column of images indicates the column sampled in the plots at the right. Panel (A): A cosmic ray strike in a deep space part of the image leaves a trail of photoelectrons in the readout direction. The trail shows up as higher levels in the uncorrected FLT data (blue trace) compared to the corrected FLC data (pink trace). The difference plot in the right column shows that the correction takes counts out of the trail (negative values at rows <1690) and restores them to the core of the cosmic ray strike (positive spike). This is the desired result of the pixel-based CTE correction. Panel (B): Jupiter’s limb (here, the terminator limb) needs to be precisely located for navigation and mapping of the data. The maximum correction of $14 e^-$ (at row 1420, dashed vertical line) is about 5% of the signal, but does not noticeably affect the location of the limb. Panel (C): Complex cloud features have pixel-based CTE corrections less than 1% of the signal level (well within photometric uncertainties). Panel (D): Jupiter’s illuminated limb is much sharper than the terminator limb in panel B. This section of the image is farthest from the readout edge of the detector and, thus, has the strongest CTE effects. Still, the correction is mainly concentrated in the deep space part of the image, and the limb location is identical in both corrected and uncorrected data.

(panel C). The position of the planetary limb is used for navigation and is found to be the half-power point between the on-planet brightness and surrounding space. The shifting of charge from the CTE correction acts to slightly move the half-power point in the readout direction. Panels (B) and (D) suggest this shift in the half-power point is in the range of 0.01 pixel for the sharp, illuminated limb, to 0.1 pixel for the darker terminator limb. This is smaller than our general navigational uncertainty, which has a precision of 0.25 pixel and an accuracy of ~ 0.4 pixel. Because the pixel-based CTE correction is designed to improve photometry of sparse point sources rather than extended sources, we work exclusively with the uncorrected data (FLT files).

2.6. Gyroscope Constraints

In order to manage gyroscope performance, additional observatory overheads were introduced in 2017–2018. Periodic gyro bias activities were required at regular intervals. Each gyro bias activity consists of a 20 minute procedure that must be done close to the same pointing as the target, but tracking at sidereal rates. The gyro bias activities reduce the number of science exposures per orbit that can be taken, so longitudinal coverage in some filters is less complete than other filters.

During Servicing Mission 4 in 2009, HST’s complement of six gyroscopes was refreshed, with three standard flex lead gyros (G1, G2, and G5) and three enhanced flex lead gyros (G3, G4, and G6). Normal pointing and control is performed with three gyros operating simultaneously. At the beginning of 2018, HST was operating with G1, G2, and G4, but the performance of G2

was steadily declining. After failures of G1 (2018 April 21) and G2 (2018 October 5), HST is currently operating with its three remaining gyros: G3, G4, and G6 (Osten & Brown 2018; Osten 2019). All three are of the enhanced flex lead type that are expected to have greater lifetimes than the gyros that have failed to date. During the decline of G2 performance, and as stability issues with G3 were encountered, the number of consecutive HST orbits without a bias update evolved from eight orbits to four in 2017 June, and finally to two orbits in early 2018, affecting multi-orbit coverage of PJs 12 and 19, as well as OPAL 2018 and 2019 observations of Jupiter.

2.7. Photometric Calibration

The latest photometric calibration for WFC3/UVIS (Deustua et al. 2016, 2017), called “UVIS 2.0,” includes new flat fields and normalization procedures (Mack et al. 2016) compared to the earlier “UVIS 1.0” calibration pipeline in use prior to 2016. The WFC3 quad filters (i.e., FQ889N for the Jupiter observations discussed here) have not been updated, so we have included an estimated 3% reduction in calibrated fluxes in quad filters, based on average changes in photometric calibrations for other filters between the UVIS 1.0 and 2.0 calibration systems. Photometric uncertainties in the UVIS 2.0 calibration are estimated to be 1.2%–1.3% (Deustua et al. 2016, 2017).

Calibrated HST data are images with data numbers corresponding to count rates in units of $e^- s^{-1}$, and the FITS header keyword PHOTFLAM gives the inverse sensitivity factor to convert to spectral irradiance units of $erg cm^{-2} s^{-1} \text{\AA}^{-1}$. But for solar system science in the NUV–NIR

range, reflectance in I/F units is commonly used. To convert the image data units of $e^- s^{-1}$ to I/F , we provide a FITS header keyword PHOTIF and its uncertainty, SIG_PHOT, such that

$$\text{PHOTIF} = \text{PHOTFLAM}/(\Omega F_{\odot}),$$

where Ω is the solid angle of a WFC3/UVIS pixel with default *astrodrizzle* parameters ($0.03962^2 \text{ arcsec}^2$), and πF_{\odot} is the solar spectral irradiance at Jupiter's orbital distance at the time of the exposure within the bandpass of the spectral element. To calculate πF_{\odot} , we use the Colina et al. (1996) solar spectrum, the heliocentric distance from the JPL Horizons ephemeris system,¹³ and spectral element throughput curves available directly for download from STScI.¹⁴ The SIG_PHOT uncertainty in our I/F calibration is dominated by a systematic 5% uncertainty in the solar spectrum (Colina et al. 1996), but also includes a 1% error typical of photometric zero-point uncertainty (Deustua et al. 2017).

2.8. Temporal Coverage

Although most HST observations had timing linked to Juno perijoves, there are two exceptions. Observations in the Outer Planet Atmospheres Legacy (OPAL) program were taken near solar opposition, to maximize spatial resolution at Jupiter (Simon et al. 2015). OPAL 2017 observations happened very close to perijove 5.

A cluster of imaging observations in 2017 January were planned to coincide with a Juno perijove, under the original plan with 14 day Juno science orbits. When Juno was instead kept on a 53 day orbit (Bolton et al. 2017), the 2017 January observations at a number of observatories (including the VLA) were not reschedulable (de Pater et al. 2019b). We include the 2017 January data from HST and Gemini in this report for two reasons: they have high intrinsic scientific value (in part due to the wide range of multiwavelength Jupiter observations planned during that time period), and they are still highly relevant to Juno because they document Jupiter's conditions as they evolve over the planned 5 yr Juno mission.

Table 3 lists the timing of both the HST and Gemini data reported here. The timing of Juno perijove passes is given in Table 4. Some HST observations had to be offset by one or two Jupiter rotations due to limited guide star availability or due to accommodation of the Juno-related UV auroral imaging program (Grodent et al. 2018). Perijoves 5, 11, and 12 fell close to OPAL observations. Figure 3 gives a graphical summary of the temporal coverage of the data, compared to the Juno perijove sequence. On PJ 22, HST unfortunately missed the Juno longitude due to human error.

3. Gemini NIRI M -band Imaging Data

We use the NIRI instrument at Gemini North Observatory to obtain high-resolution imaging of Jupiter in the $5 \mu\text{m}$ wavelength range (Hodapp et al. 2003). Specifically, we use the M' filter, with a central wavelength of $4.68 \mu\text{m}$ and a spectral width of $0.24 \mu\text{m}$ (technical information is listed at <https://www.gemini.edu/sciops/instruments/niri>). At this wavelength, only NIRI's $f/32$ camera with its $22''.4$ square field of

view can be used, because the larger angular pixel size using the $f/6$ and $f/14$ cameras causes saturation before the minimum detector readout time. Some preliminary NIRI data from this program have been previously published (Fletcher et al. 2018; de Pater et al. 2019a; Marcus et al. 2019), but details of the data analysis have been deferred to this paper.

3.1. Mosaic Patterns

Jupiter's angular diameter ranges from about $32''$ to $50''$ depending on geocentric distance, so a pattern of mosaic steps is required in order to image the entire planet with the $22''.4$ FOV of NIRI. Sizes of the mosaics range from 2×2 to 3×3 (Table 3). The maximum Jupiter equatorial diameter for a 2×2 mosaic is $40''.5$, and the maximum diameter for a 3×2 mosaic is $43''.2$ (3×3 mosaics are used for the largest apparent diameters). Panel A of Figure 4 shows a sample mosaic layout for the 2×2 case. Each on-target mosaic position consists of 38 individual exposures.

Interspersed with mosaic steps are sets of sky frames, needed to characterize the time-variable background brightness. Sky frames include $3''$ offsets to eliminate any background sources that may be present, and a series of at least nine sky frames is needed to ensure that persistence (from the previous Jupiter frames) does not affect the sky exposures. In addition to creating background corrections, we used the sky frames to generate maps of dead and nonlinear pixels. In the final mosaics, these bad pixels were filled by dithering that was fortuitously introduced by telescope pointing jitter.

Mosaics were streamlined for 2018. Earlier observations (2016 and 2017) involved three sets of 38 exposures each at every mosaic pointing (with sky sets between each set). This ensured that variable sky conditions on timescales of 5–10 minutes did not adversely affect the data. But for later observations, we decided to prioritize efficiency by taking only a single set of 38 exposures at each mosaic pointing.

3.2. Lucky Imaging

The diffraction limit of the $D = 8.1 \text{ m}$ Gemini telescope at $4.7 \mu\text{m}$ is $1.22\lambda/D = 0''.15$. Unfortunately, adaptive optics (AO) cannot be used with NIRI at this wavelength, because the current design of the ALTAIR AO system (Christou et al. 2010) contributes significant thermal background, and the dichroic beamsplitter only transmits light out to $4.1 \mu\text{m}$. A new beamsplitter that transmits out to $5 \mu\text{m}$ is being evaluated (Trujillo et al. 2013). Currently, lucky imaging is the only option for recovering the diffraction limit, by taking a series of frames and keeping only the sharpest ones. We use 10% as a guide for the fraction of frames to keep. Adding more frames does increase signal-to-noise but does little to improve image quality; using a smaller fraction is not effective for removal of imaging artifacts (Figure 4).

Deciding which frames to use can be challenging, when hundreds of exposures are taken in a night. As a first step, we sort all 38 images taken at a single mosaic pointing, ranked by a custom Sobel Image Quality metric. The images ranked in the top 10% are examined to find the best single image, which serves as the key frame for the set.

Our Sobel IQ metric is based on the Sobel filter, an image transformation using a 3×3 pixel gradient operator to enhance edges in images (e.g., Danielsson & Seger 1990). We generate the Sobel IQ metric using the following steps:

¹³ JPL Horizons URL is <https://ssd.jpl.nasa.gov/?horizons>.

¹⁴ WFC3/UVIS throughputs are at <http://stsci.edu/~WFC3/UVIS/System/Throughput> or <http://stsci.edu/hst/instrumentation/wfc3/performance/throughputs>.

Table 3
Timing of HST/WFC3 and Gemini-N/NIRI *M*-band Imaging Observations

Juno PJ ^a	Start (UTC)	Decimal Year	Span (hr) ^b	Number of Frames ^c	Instrument	Program ID ^d
...	2016 Feb 09 09:35	2016.107	19.6	117	WFC3	GO-14334
3	2016 Dec 11 08:01	2016.943	25.6	172	WFC3	GO-14661
3	2016 Dec 14 14:21	2016.951	2	2 × 2	NIRI	GN-2016B-FT-18
...	2017 Jan 11 09:20	2017.029	14.9	124	WFC3	GO-14839
...	2017 Jan 11 14:10	2017.029	2.4	2 × 2	NIRI	GN-2016B-FT-18
...	2017 Jan 12 13:03	2017.031	3.5	2 × 2	NIRI	GN-2016B-FT-18
...	2017 Jan 23 12:19	2017.062	4.2	2 × 2	NIRI	GN-2016B-FT-29
4	2017 Feb 01 15:28	2017.086	21.4	154	WFC3	GO-14661
4	2017 Feb 01 15:40	2017.086	0.9	2 × 2	NIRI	GN-2017A-Q-60
4	2017 Feb 05 14:12	2017.097	2	2 × 2	NIRI	GN-2017A-Q-60
5	2017 Mar 27 07:03	2017.234	0.6	10	WFC3	GO-14661
5	2017 Apr 03 01:11	2017.253	21.2	105	WFC3	GO-14756
6	2017 May 19 14:38	2017.379	0.6	10	WFC3	GO-14661
6	2017 May 21 05:34	2017.384	1.4	3 × 2	NIRI	GN-2017A-Q-60
7	2017 Jul 09 07:00	2017.518	1.3	2 × 2	NIRI	GN-2017A-Q-60
7	2017 Jul 10 06:17	2017.521	0.9	2 × 2	NIRI	GN-2017A-Q-60
7	2017 Jul 11 09:25	2017.524	0.6	14	WFC3	GO-14661
11	2018 Feb 06 17:20	2018.099	0.7	17	WFC3	GO-14661
11	2018 Feb 07 09:43	2018.102	8.2	44	WFC3	GO-14936
12	2018 Apr 01 08:38	2018.247	16.4	78	WFC3	GO-14661
12	2018 Apr 01 10:31	2018.247	0.8	3 × 2	NIRI	GN-2018A-Q-202
...	2018 Apr 17 01:15	2018.291	19.8	111	WFC3	GO-15262
13	2018 May 24 14:23	2018.392	0.6	10	WFC3	GO-14661
13	2018 May 26 07:38	2018.398	3.1	3 × 3	NIRI	GN-2018A-Q-202
13	2018 May 27 10:17	2018.401	1.6	3 × 3	NIRI	GN-2018A-Q-202
14	2018 Jul 16 06:00	2018.537	2.8	3 × 2	NIRI	GN-2018A-Q-202
14	2018 Jul 16 13:47	2018.537	0.6	10	WFC3	GO-15159
15	2018 Sep 07 00:13	2018.682	0.7	6	WFC3	GO-14661
18	2019 Feb 12 15:59	2019.116	0.7	16	WFC3	GO-14661
19	2019 Apr 06 10:29	2019.261	3.8	18	WFC3	GO-15665
19	2019 Apr 06 12:23	2019.261	2.5	3 × 2	NIRI	GN-2019A-Q-202
19	2019 Apr 07 10:19	2019.264	3.8	20	WFC3	GO-15665
19	2019 Apr 07 14:57	2019.264	0.7	3 × 2	NIRI	GN-2019A-Q-202
19	2019 Apr 08 10:09	2019.266	3.8	20	WFC3	GO-15665
19	2019 Apr 08 14:21	2019.266	0.6	3 × 2	NIRI	GN-2019A-Q-202
19	2019 Apr 09 08:23	2019.269	16.6	47	WFC3	GO-14661, 15159
19	2019 Apr 09 09:59	2019.269	3.8	19	WFC3	GO-15665
20	2019 May 28 12:38	2019.403	0.7	3 × 3	NIRI	GN-2019A-Q-202
20	2019 May 29 09:30	2019.406	0.7	3 × 3	NIRI	GN-2019A-Q-202
...	2019 Jun 25 07:31	2019.480	3.3	3 × 3	NIRI	GN-2019A-Q-304
...	2019 Jun 26 08:14	2019.483	21.3	111	WFC3	GO-15502
21	2019 Jul 21 13:42	2019.551	0.6	10	WFC3	GO-14661
22	2019 Sep 12 08:04	2019.696	0.6	14	WFC3	GO-14661

Notes.

^a Some observations are relevant to the Juno time period, but were not scheduled close to a Juno perijove pass. Perijoves 1–2, 8–10, and 16–17 were not observed due to Jupiter’s proximity to the Sun in the sky.

^b Span is the full duration from first to last exposure without regard to program interruptions.

^c For HST, number of frames is the count of all successful separate exposures within the set. For Gemini, the value gives the size of the mosaic pattern. Gemini observations with spans longer than 1 hr indicate repeated mosaic patterns as Jupiter rotated.

^d Program IDs can be used to obtain raw data from the HST archive at <https://archive.stsci.edu/> or the Gemini archive at <https://archive.gemini.edu/>.

1. Create a Sobel-filtered image from the key frame for a set of images.
2. Take a histogram of the pixel values in the filtered key frame image.
3. Determine the cutoff value within the filtered image. We empirically chose a value 10% larger than the half-width above the maximum in the histogram (approximately one sigma above the mean in the filtered image, if the distribution were Gaussian).

4. The number of pixels within the filtered image that are above the cutoff value is the Sobel IQ metric in our technique (y-axis of Figure 4).

The best images within a single mosaic pointing set are coadded to improve S/N and image quality. Each individual frame takes about 5.5 s for exposure and readout, so a full set of 38 frames takes about 3.5 minutes. In this amount of time, Jupiter’s rotation would cause a point at disk center to move by about 0.74 (34 pixels), so images cannot be simply stacked in

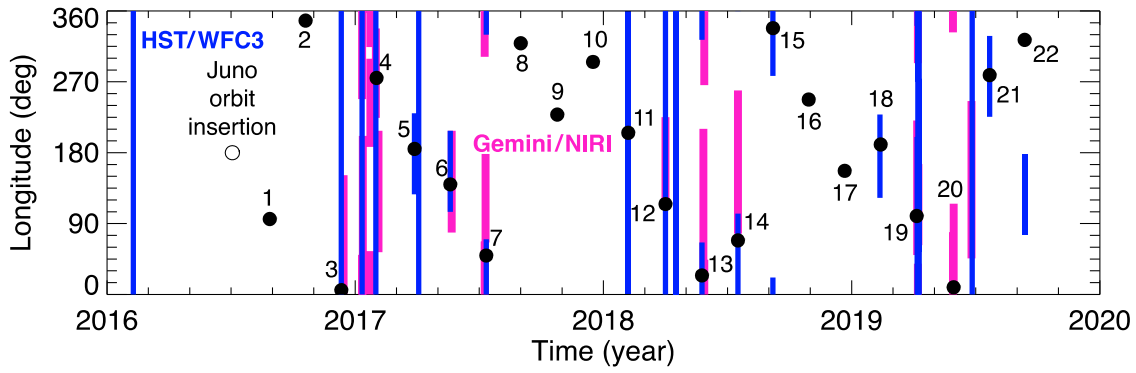


Figure 3. Longitudinal coverage of imaging data from HST (blue) and Gemini (light red), compared with Juno perijove longitudes (numbered black circles). Imaging data are missing for times when Jupiter’s solar elongation angle was $<50^\circ$.

Table 4
Juno Perijove Times and Geometric Parameters

Juno PJ	Time (UTC) ^a	Decimal Year	Longitude (deg) ^b	Solar Elongation (deg) ^c	One-way Light Time (minutes) ^d
JOI	2016 Jul 05 02:47:32	2016.508	32.7	64.1	48.3
1	2016 Aug 27 12:50:44	2016.653	95.8	22.6	53.0
2	2016 Oct 19 18:10:54	2016.798	347.7	18.2	53.1
3	2016 Dec 11 17:03:41	2016.943	5.5	61.6	48.7
4	2017 Feb 02 12:57:09	2017.089	274.9	110.8	41.8
5	2017 Mar 27 08:51:52	2017.234	184.9	167.1	37.2
6	2017 May 19 06:00:47	2017.379	139.8	135.4	39.0
7	2017 Jul 11 01:54:42	2017.524	49.4	85.7	45.2
8	2017 Sep 01 21:48:50	2017.666	319.0	42.5	51.1
9	2017 Oct 24 17:42:31	2017.811	228.4	1.9	53.5
10	2017 Dec 16 17:56:59	2017.956	295.3	40.8	51.1
11	2018 Feb 07 13:51:30	2018.102	205.1	86.9	44.8
12	2018 Apr 01 09:45:43	2018.247	114.6	139.2	38.4
13	2018 May 24 05:39:50	2018.392	24.0	163.4	36.8
14	2018 Jul 16 05:17:39	2018.537	68.7	109.7	41.3
15	2018 Sep 07 01:11:57	2018.682	338.2	63.6	47.8
16	2018 Oct 29 21:06:17	2018.825	247.6	21.5	52.2
17	2018 Dec 21 17:00:27	2018.970	157.0	20.2	52.1
18	2019 Feb 12 17:34:16	2019.116	235.3	64.0	47.4
19	2019 Apr 06 12:14:00	2019.261	99.7	112.1	40.4
20	2019 May 29 08:08:14	2019.406	9.1	166.7	35.9
21	2019 Jul 21 04:02:44	2019.551	278.6	137.1	37.4
22	2019 Sep 12 03:40:47	2019.696	323.3	86.9	43.5

Notes.

^a Time listed is spacecraft event time (SCET) at the moment of perijove.

^b Longitude listed is for the spacecraft position at the moment of perijove.

^c One-way light time is for geocentric observer location.

detector or sky coordinate space. Rotational blurring is not significant within a single 0.3 s exposure (0.05 pixel displacement at disk center), but among frames at one mosaic pointing, stacking must be done in latitude/longitude coordinate space. We apply linear shifts in latitude/longitude during the stacking process to minimize navigational errors between the individual frames. The most challenging case for navigating the images is for the central contributor to a 3×3 mosaic. In these images, the limb is not visible, and navigation is done by aligning tie points to previously navigated images that do contain Jupiter’s limb, using procedures described in Lii et al. (2010).

3.3. Temporal Coverage

Temporal coverage within the NIRI data set is given in Table 3 and Figure 3. In some cases, offsets between Gemini

and Juno timings by a couple of days were caused by unavailability of the NIRI instrument at Gemini North (it shares a port with NIFS), or due to difficulties observing the appropriate Juno longitude on Jupiter while the planet is at high enough elevation at night. Observations were attempted on 2018 February 9 near Juno’s PJ11, but high winds rendered the data unusable (no sharp frames were obtained). The raw data are available in the Gemini archive, but these observations are not reported here due to their poor quality.

3.4. Additional High-resolution IR Imaging Programs

Observing programs are being conducted by other teams to image Jupiter during Juno spacecraft passes. The VISIR imager at ESO’s Very Large Telescope (VLT), operated in burst mode to obtain lucky-imaging data also in the $5 \mu\text{m}$ range, has

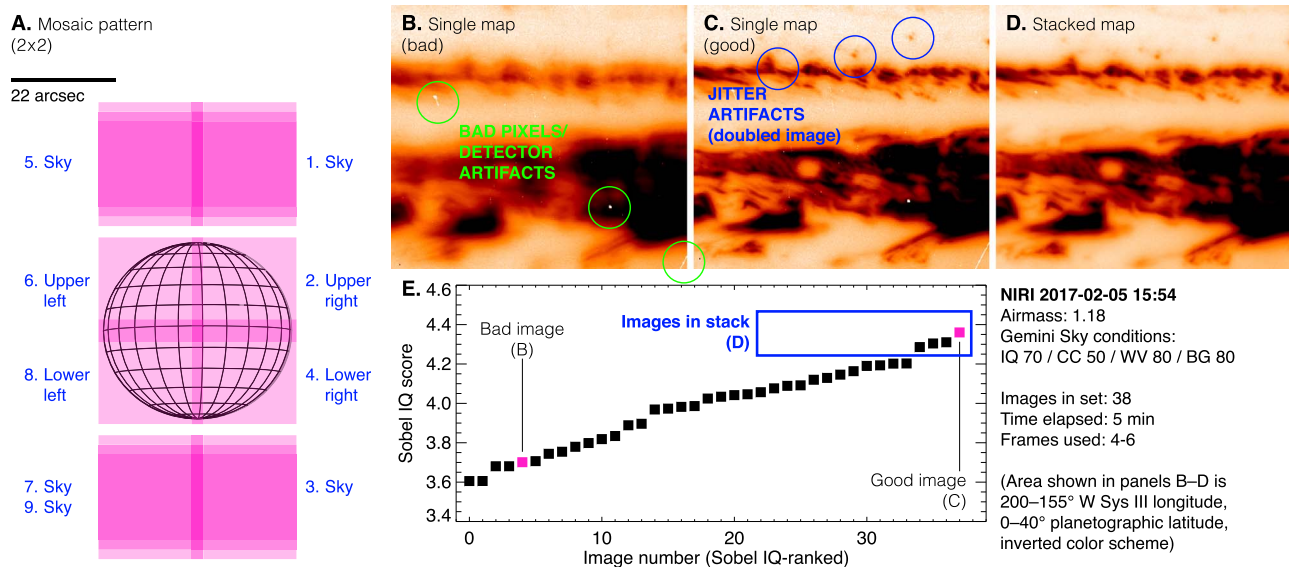


Figure 4. Lucky imaging procedure for building Gemini/NIRI Jupiter mosaics. Panel (A): Mosaic layout includes $\sim 2''/6$ overlap between the 2×2 on-source pointings, and dithered sky frames between each mosaic step. Panels (B) and (C): Individual NIRI images are affected by variable seeing, which can produce a blurred image, or a sharp but “double” image. Detector artifacts and bad pixels can also be seen in single frames. Panel (D): After the best frames are converted to cylindrical maps and stacked in latitude–longitude space, we obtain a finished lucky-imaging mosaic pointing. Panel (E): We use the Sobel image quality metric to rank all 38 frames within a single mosaic step and select the best $\sim 10\%$ for inclusion in the final mosaic.

obtained imaging data at several perijove times (Fletcher et al. 2018). This VLT data set includes longer-wavelength imaging, further discussed in Section 5.5. NIRI is also being used to obtain near-IR images in reflected sunlight with the ALTAIR AO system, observing Jupiter at Juno-relevant times when Galilean satellites are available as natural guide stars (Giles et al. 2019). Data from the VLT and NIRI AO programs are not included as part of the archive collections described in Section 4.

4. High-level Science Products in the WFCJ Archive Collection

A major motivation for this paper is to serve as a guide for HLSPs available from this program. The HLSPs are distributed across two nodes at STScI’s MAST archive site. The Wide Field Coverage for Juno (WFCJ) program node contains HST and Gemini *M*-band HLSPs associated with Juno perijove passes,¹⁵ including WFC3 and NIRI imaging data taken in direct support of VLA Jupiter observations. The OPAL program node contains HLSPs associated with annual Jupiter observations conducted near solar opposition for maximum spatial resolution.¹⁶

The HLSP collections are dynamic and designed for growth, since new data for WFCJ will be collected over the Juno mission, and we expect that data for OPAL will be collected as long as HST’s imaging capability remains functional. HLSPs available at these nodes are versioned, so older data are still available. The main interface serves the most recent version of all data products. New data products may be available in the future, but this paper describes the types of HLSPs currently available at these archive nodes. Figure 5 gives a graphical example of the content of the NAV HLSP type, and Table 5 summarizes the various types available:

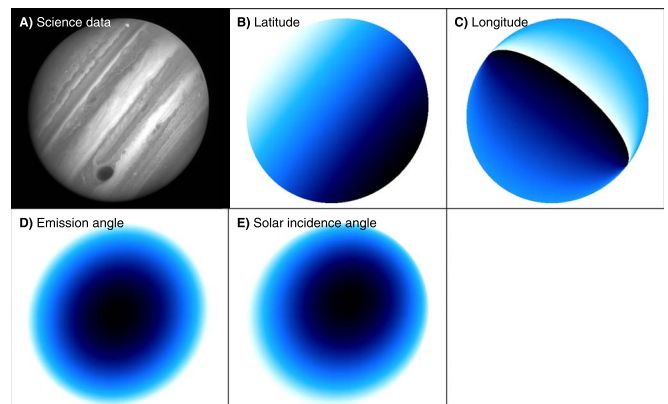


Figure 5. Several types of HLSPs available at the MAST archive include supporting data in backplanes (as FITS extensions). Shown here are backplanes of latitude, longitude, emission angle, and solar incidence angle data that are part of a NAV format HLSP. Details of each science product type are given in Section 4 and summarized in Table 5.

1. NAV files are cleaned, I/F -calibrated, navigated individual image frames in sky coordinates. They are multi-extension FITS format binary files with extensions providing metadata, reflectance, latitude (planetographic), longitude, emission, and incident angle for each image pixel. The basic processing of HST data is performed with STScI packages available in the AstroConda distribution. Single images are cleaned as thoroughly as possible for cosmic rays using the LA-Cosmics routine based on Laplacian filtering (van Dokkum 2001), and corrected for fringing if necessary (Section 2.2). Geometric distortion is corrected as described in Section 2.3. Navigation to sub-pixel accuracy is performed with the Simnav method (Lii et al. 2010), which aligns the real data with synthetic Jupiter images (including limb darkening and convolved with the WFC3/UVIS

¹⁵ WFCJ HLSPs are available in doi:10.17909/T94T1H.

¹⁶ OPAL HLSPs are available in Simon (2015).

Table 5
High-level Science Product Format Information

Science Product Type	Backplanes ^a	Spatial Coordinates	File Format	Source	Archive Node ^b
NAV	Latitude Longitude Emission angle Incidence angle	Sky	FITS	WFC3	WFCJ
REG	Emission angle Incidence angle	Latitude/longitude	FITS	WFC3	WFCJ
GLOBALMAP	None	Latitude/longitude	FITS, TIFF, PNG, JPG	WFC3	OPAL, WFCJ
MOSAIC	Emission angle Incidence angle	Latitude/longitude	FITS, JPG PDF	NIRI	WFCJ
POLAR	Latitude Longitude Emission angle Incidence angle science image ^c	Polar-projected latitude/longitude	FITS, JPG	WFC3	WFCJ
ZWP	None	Latitude	ASCII, FITS	WFC3	WFCJ
MWRTRACKS ^d	None	Latitude/longitude	PNG, JPG	Juno	None

Notes.

^a Backplanes are present as extensions in FITS format data.

^b Individual data sets are archived under OPAL or WFCJ archive nodes (Simon 2015 and doi:10.17909/T94T1H, respectively), depending on observing program numbers (see Tables 1 and 3). HST programs in support of VLA observations are included as part of the WFCJ archive node.

^c Uncorrected (for limb darkening) science image data are provided for single-image polar projections but not for polar mosaics where multiple frames (with data at different viewing angles) have been combined.

^d MWRTRACKS data are only shown as part of preview images on the WFCJ archive node; digital data files with this information in map format are not available outside of the Juno team.

point-spread function obtained from TinyTim¹⁷), based on geometric parameters from JPL Horizons.

2. *REG* files are individual regridded cylindrical projections of individual NAV files in longitude–latitude coordinates. *REG* files are multi-extension FITS format binary files with extensions providing metadata, emission, and incident angle. Latitude coordinates are in the planetographic system, but planetocentric maps can be provided upon request.
3. *GLOBALMAP* files are maps in longitude–latitude coordinates, combined from multiple cylindrically mapped exposures. Limb-darkening coefficients k are given in the README files associated with the data sets at the archive nodes, and k varies with filter (and sometimes with epoch). Values of k are chosen to maximize the aesthetic result in the *GLOBALMAP* output products. The limb-darkening functional form is a Minnaert function, as described in, e.g., Wong et al. (2018). The *GLOBALMAP* image sizes are selected to span 360° of west longitude and 180° of planetographic latitude. There are no emission/incident angle extensions in the *GLOBALMAP* files because viewing angle data have been corrected by the limb-darkening function. Theoretically, *GLOBALMAP* HLSPs could be generated by combining *REG* files, but practically, they have been generated for these programs by a separate process (Simon et al. 2015).
4. *MOSAIC* maps in longitude–latitude coordinates are similarly created from individual Gemini *M*-band maps. We do not host NAV or *REG* files from the Gemini data,

because these are based on individual frames before stacking in the lucky-imaging approach (Section 3.2). We use a different name from *GLOBALMAP* for these products simply because it is rarely possible to create a full global map of Jupiter from a ground-based observatory. HST’s 96 minute orbit provides an advantage in this respect over the 24 hr rotation period of the Earth.

5. *POLAR* files are polar-projected views of the north and south poles. Like NAV data, *POLAR* data are multi-extension FITS format binary files with extensions providing metadata, reflectance, latitude, longitude, emission, and incident angle for each image pixel. To ensure readability to the eye, individual frames and polar mosaics are all corrected for limb darkening, with limb-darkening coefficients encoded in the metadata. An additional backplane containing the original science data (without limb-darkening correction) is provided for single-frame polar projections. This backplane is not provided for polar mosaics, since those stack multiple frames at different original viewing geometries.
6. *ZWP* files are zonal wind profiles (ZWPs) derived by horizontal image correlation in data spanning two Jovian rotations. Thus, ZWPs are not available at every epoch. *ZWP* HLSPs are hosted in text (ASCII) and FITS format tables, with metadata and four columns of data. Column 1 is the latitude in planetographic coordinates. Column 2 is the eastward velocity in units of m s^{-1} . Column 3 is the uncertainty in the velocity. Column 4 is the number of tie points used to derive the uncertainty; a low number of tie points indicates a poorly determined uncertainty.

¹⁷ TinyTim URL is <http://tinytim.stsci.edu/cgi-bin/tinytimweb.cgi>.

The method for deriving ZWPs and estimating their uncertainties is described in Asay-Davis et al. (2011) and Tollefson et al. (2017).¹⁸

7. *MWRTRACKS* are graphically shown on some preview images at the WFCJ archive node. These tracks indicate Juno’s path over Jupiter’s 1 bar surface during a specific perijove pass. Juno tracks are similarly shown in Figures 8, 9, and 11 in Section 5, and in Figures 20–24 of Janssen et al. (2017). On passes optimized for MWR measurements, these tracks are composed of nadir footprints. On other passes, the tracks show minimum (but nonzero) emission angles observed by MWR during each spacecraft rotation. In many cases, the HST or Gemini images were acquired significantly before or after the Juno MWR measurements. In these cases, the footprint tracks have been advected by the ZWP to form somewhat twisted paths. For this purpose, we use the ZWP measured closest in time to the observations. The twisted paths pass over the same features in the map images that Juno measured (under the assumption that all motions are zonal).
8. *COMPOSITES* show multiple wavelengths of data mapped to the visual channels of the color image representations. Different filter mappings have been created to display optical color, cloud height, or ultraviolet reflectivity. Figures in Section 5 make use of color composites. Because a wide range of combinations can be created from the observations, composites are typically not archived as HLSPs. Instead, users may obtain data in separate filters and create composites on their own. One exception is RGB color composites (typically from F631N, F505N, and F395N) of GLOBALMAP data, which are available in TIF image format on the OPAL and WFCJ archive nodes. Composites may be created in sky coordinates to show Jupiter’s full disk, or in longitude–latitude coordinates to show atmospheric maps. RGB color composites are simply created by loading one exposure per color channel, but more advanced methods (Rector et al. 2007) can be used to customize color schemes or display any number of images in separate wavelengths.

5. Results

Although this paper provides an overview of the data set and a thorough description of the data reduction processes, early releases of the data have already been published in focused scientific studies. In this section, we describe some of the early science results and provide updates to ongoing research in the studies of zonal winds, atmospheric waves, convective storms, the GRS, cyclonic vortices, and polar phenomena.

5.1. Zonal Winds

ZWPs derived from programs listed in Table 3 have been recently published. Tollefson et al. (2017) analyzed the temporal variability of Jupiter’s ZWP, extending the results of Simon-Miller & Gierasch (2010) and Asay-Davis et al. (2011). Notably, Tollefson et al. (2017) demonstrated mean uncertainties of $\sim 6 \text{ m s}^{-1}$ in the zonal wind speed using WFC3 data, about a factor of two better than was possible with the previous-generation WFPC2 camera on HST. Johnson et al. (2018) quantified spatial variation in zonal flow, finding

significant changes in jet speeds and latitudes at different locations around the planet, and Hueso et al. (2017) showed consistency between ZWPs derived from 2016 WFC3 and ground-based imaging (albeit with a factor of two larger standard deviation in the ground-based profile).

Simon-Miller et al. (2007) and Simon-Miller & Gierasch (2010) found hints of periodic variation in Jupiter’s ZWP, depending on the data sets included in the analysis. They used Lomb–Scargle periodograms to search for significant periodic signals at specific latitudes. One particular issue was limited coverage of short-timescale variability. A significant equatorial variation with a period near 12 yr was seen in a 14 yr HST/WFPC2 data set that included a 2007 March ZWP, but it was not seen in an identical data set that included 2007 February instead of 2007 March (Simon-Miller & Gierasch 2010). Tollefson et al. (2017) found a similar significant equatorial periodicity (at 13.8 yr instead), using a 22 yr data set that combined ZWPs derived from both WFPC2 and WFC3 data. Given the influence of data sets with short time separations on the periodogram results, we used several new ZWPs derived from WFC3 data to augment the Tollefson et al. (2017) data set, reaching a total duration of 25 yr (excluding Voyager) and containing more short time separations within the 2017–2019 period. Figure 6 shows the time series and resulting periodograms, using all available data (top) or a subset of data omitting any ZWPs within 5 months of another ZWP closer to opposition. The particular ZWPs used in Tollefson et al. (2017), and in each row of Figure 6, are listed in Table 6. Periodograms corresponding to additional subsets listed in Table 6 are available in the Appendix. The periodograms are based on ZWPs like those in Figure 7(A), smoothed to one-degree latitudinal resolution.

Very close to the equator ($\pm 4^\circ$ latitude), significant periodicities (with orange/red colors indicating false-positive probabilities < 0.2) can be seen in the subset of data omitting close time separations (lower row of Figure 6). The variability has characteristic periods in the range of 6–7 and 14 yr, very similar to variability in $5 \mu\text{m}$ infrared brightness in equatorial regions recently with periodicities of 6–8 or 13–14 yr (Antuñano et al. 2018). Temporal overlap is not precise between the spacecraft ZWP data set and the ground-based $5 \mu\text{m}$ data set of Antuñano et al. (2018). Equatorial disturbances, or $5 \mu\text{m}$ brightening events, were seen in 1999 December and 2007 February, and persisted for 12–18 months. At approximately these times, near-equatorial wind speeds were faster than usual. Antuñano et al. (2018) predicted a new equatorial disturbance in the 2019–2021 time range, but the equatorial region still had not brightened significantly by late 2019 at $5 \mu\text{m}$ wavelengths (Figure 8(A)), although Figure 8(B) shows that it darkened from its typical white coloration to the more reddish tint in 2018 and 2019. The equatorial wind profile remained largely constant from 2016 to 2019, with peak jet speeds at 7°S of $142\text{--}147 \text{ m s}^{-1}$ in all but one epoch and no significant increasing trend. The “Subset 2018” periodogram (Figure 15) has a more significant near-equatorial signal at periods near 7 and 14 yr, compared with the “Subset” periodogram in Figure 6 (bottom) that includes the 2019 data. Thus, the lack of equatorial variation in 2019 seems to break the trend otherwise seen in the zonal wind data, as well as in the $5 \mu\text{m}$ brightness data of Antuñano et al. (2018).

Periodic variability in measured zonal winds could be a change in the true wind speed at constant altitude, but is more likely to be an indication of vertical wind shear: the clearing of high-level clouds responsible for the $5 \mu\text{m}$ brightening in

¹⁸ Versions of these profiles in planetocentric latitude coordinates are available on request.

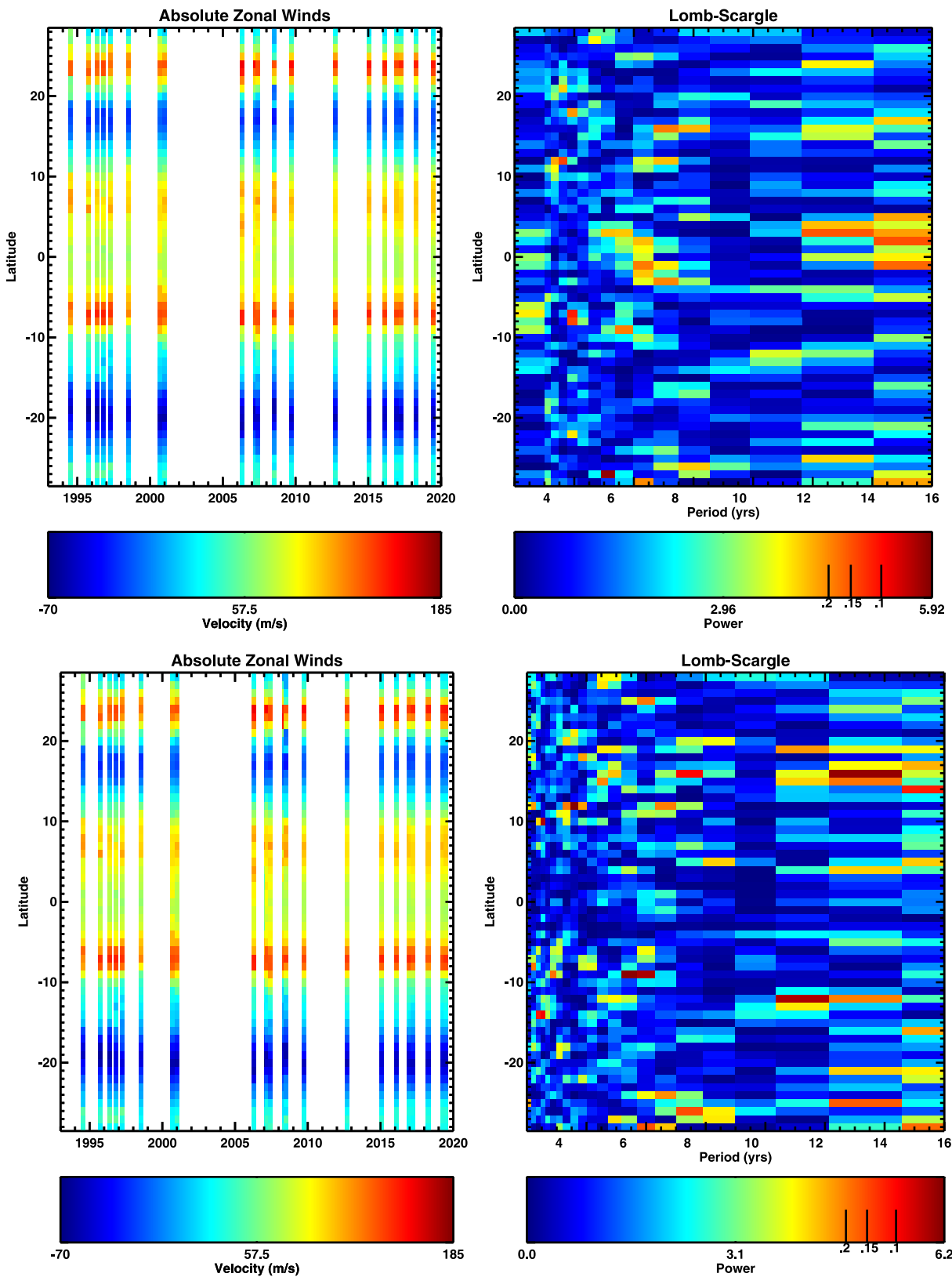


Figure 6. Different groups of zonal wind profiles data sets show consistent signs of periodic variability (see Section 5.1). Top panels: All ZWPs from Voyager in 1979 to HST in 2019 are used. Bottom panels: ZWPs are omitted when they are separated by <5 months from another profile and when they are derived from lower-resolution data than the other profile (column labeled “Subset” in Table 6). Left column panels: Zonal winds from spacecraft imaging obtained with Voyager, Cassini, and HST, with wind speeds as a function of time and latitude shown as color values. Right column panels: Lomb–Scargle periodograms based on the wind profiles, with power as a function of period and latitude shown as color values. False alarm probabilities of 20%, 15%, and 10% are shown as vertical ticks on the color bar. Individual periodogram pixels are centered on their periods.

Table 6
Zonal Wind Profiles Included in Tollefson et al. (2017), Figure 6 (“All” and “Subset” Columns), and Figures 14–20 in the Appendix (Remaining Columns)

Date	Tollefson et al. (2017) ^a	All ^b	Subset ^c	Subset 2018 ^d	HST Only ^e	WPC2 + WFC3 ^f	WFC3 only	HST Only (Filtered) ^g	WFPC2 + WFC3 (Filtered) ^h
1979.42	X	X	X	X					
1994.55	X	X	X	X	X	X		X	X
1995.76	X	X	X	X	X	X		X	X
1996.37	X	X	X	X	X	X		X	X
1996.81	X	X	X	X	X	X		X	X
1997.26	X	X	X	X	X	X		X	X
1998.54	X	X	X	X	X	X		X	X
2000.68	X	X	X	X	X	X		X	X
2001.02	X	X	X	X					
2006.31	X	X	X	X	X			X	
2007.16		X			X	X			
2007.23	X	X	X	X	X	X		X	X
2007.43	X	X	X	X	X	X		X	X
2008.38		X			X	X			
2008.52	X	X	X	X	X	X		X	X
2009.72	X	X	X	X	X	X	X	X	X
2012.72	X	X	X	X	X	X	X	X	X
2015.05	X	X	X	X	X	X	X	X	X
2016.11	X	X	X	X	X	X	X	X	X
2016.95	X	X	X	X	X	X	X	X	X
2017.03		X			X	X	X		
2017.09		X			X	X	X		
2017.25		X	X	X	X	X	X	X	X
2018.25		X			X	X	X		
2018.29		X	X	X	X	X	X	X	X
2019.27		X	X		X	X	X	X	X
2019.49		X			X	X	X		

Notes.^a List of data sets used in Figure 10 of Tollefson et al. (2017).^b List of data sets used in Figure 6 (top row).^c Subset of data sets (Figure 6, bottom row), omitting profiles separated by <5 months from another profile derived from higher-resolution data.^d Same as previous column but omitting 2019 data.^e Subset omitting ZWPs from Voyager (Simon 1999) and Cassini (Porco et al. 2003).^f Subset of all HST data except the ZWP based on ACS imaging.^g HST ZWPs, filtered to omit profiles separated by < 5 months from another profile derived from higher-resolution data.^h HST ZWPs, filtered to omit the ZWP based on ACS imaging and profiles separated by < 5 months from another profile derived from higher-resolution data.

equatorial disturbance events may also allow deeper wind speeds to be tracked. This would be qualitatively consistent with findings of increased wind speed with depth near 7.5°N by cloud tracking (Li et al. 2006) and the Galileo Probe Doppler wind experiment (Atkinson et al. 1998), justifying the assumption in Marcus et al. (2019) that vertical wind shear is similar from 7.5°N to the equator in the 1–13 bar pressure range. The 6–7 yr periodicity is weaker, and the 14 yr periodicity is absent, in the periodogram analysis including all data (upper row of Figure 6). At this point, it is unclear why the addition of short-separation data would eliminate periodic signals at longer periods.

Nonperiodic changes are also evident in Jupiter’s zonal winds. Figures 7(A), (B) shows an example of ZWP changes in 2017, following a system of storms known as a South Equatorial Belt (SEB) Outbreak. A kink in the ZWP is commonly seen in the 10°–15°S area of the SEB. A series of 2017 ZWP measurements shows that following the SEB Outbreak, the kink narrowed and shifted southwards. The three ZWPs changed monotonically over a period of almost 3 months, although only the change from 2017.03 to 2017.26 was significant beyond the formal uncertainties in the ZWP. The nature of this kink, which is unique except for a possibly similar feature in the cyclonic region between 23° and 30°N,

bears further investigation in the future. The changes in the ZWP could be related to vertical wind shear revealed by changing cloud deck levels, variability across longitudinal sectors, or true changes in the overall wind speeds.

Wind speeds near 24°N are also affected by major convective outbreaks (Figure 7(C)). As reported in previous works, the peak jet speed increases to its maximum before one of these storm events, then drops dramatically after North Temperate Belt Outbreaks occur (Sánchez-Lavega et al. 2008, 2017; Hueso et al. 2017; Tollefson et al. 2017).

A practical application of ZWPs is to compare observations taken at slightly different times. We use the zonal winds to “advect” observation footprints from one observation to match nonsimultaneous imaging coverage. Figures 9 and 11 give examples of this.

5.2. Atmospheric Waves

Mesoscale waves with wavelengths of $\sim 1^\circ$ (1200 km) in Jupiter’s North Equatorial Belt (NEB) were seen in Voyager images and rediscovered in 2015 HST images (Simon et al. 2015). The waves were absent in intervening years (except for a possible sighting in 2012). Since 2015, these mesoscale

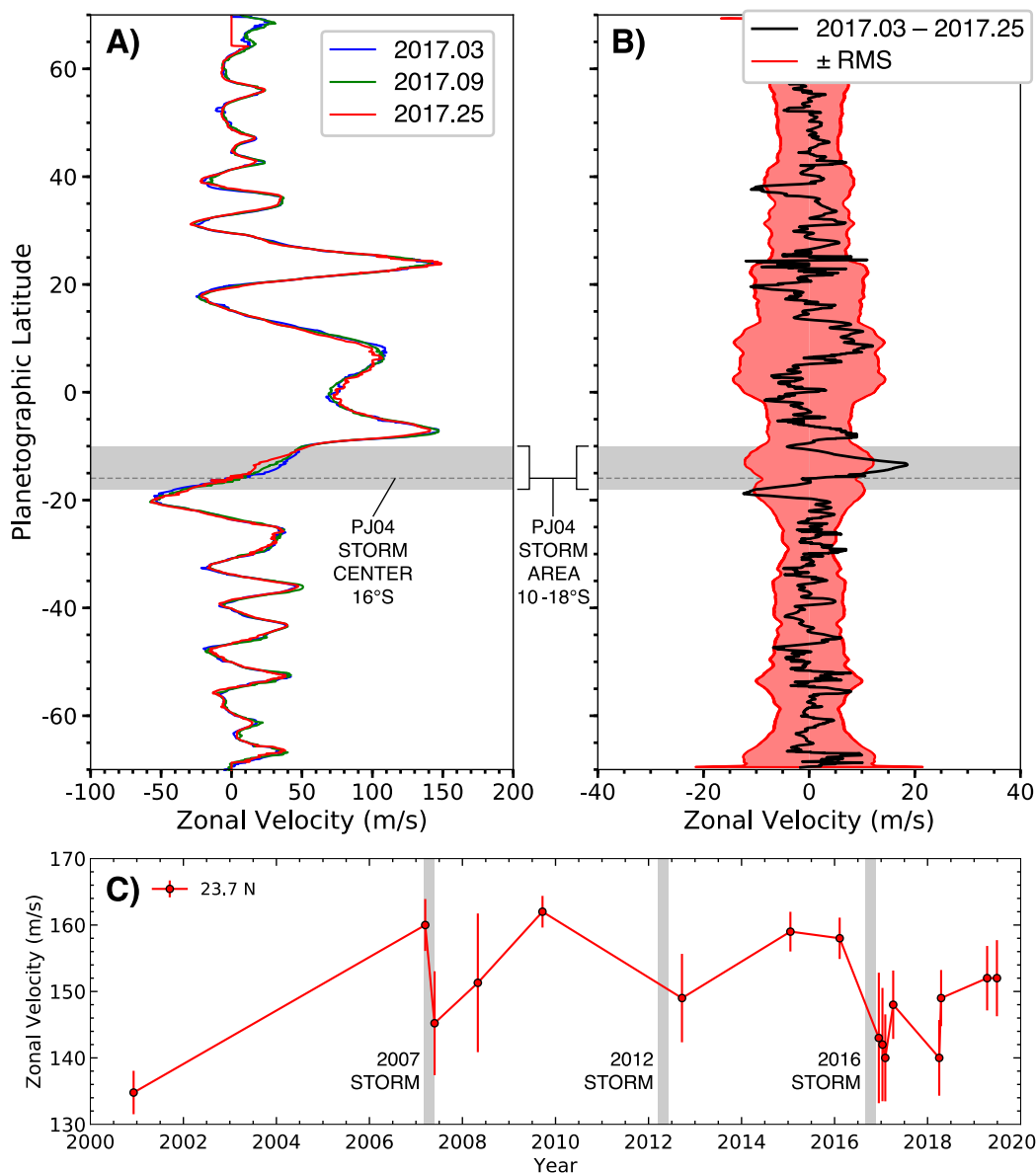


Figure 7. Variability of Jupiter’s jets is related to convective superstorms. Panel (A): A series of large convective storms in 2017 (an “SEB Outbreak”) was followed by a gradual change in the zonal wind profile near 15°S. On PJ 4, Juno passed very close to a storm that was part of the Outbreak (dashed line at 16°S). Panel (B): The difference between profiles taken 0.22 yr apart (2.6 months) is statistically significant, while differences on shorter timescales (not shown) were not greater than the rms uncertainty. Panel (C): The interaction between convective superstorms and the 23°7N eastward jet leads to a drop in jet speed, suggesting a different behavior from small turbulent eddies, whose momentum flux may maintain jets (e.g., Beebe et al. 1980; Salyk et al. 2006). Alternately, changes in cloud properties following these storms (Tollefson et al. 2017) may affect the vertical sensitivity of the wind measurements, revealing different speeds in the presence of vertical wind shear.

waves have been seen in many other data sets, even in imaging by amateur astronomers. A comprehensive study of the conditions over which these features were present from 2015 to 2018, using visible wavelength data from both HST and ground-based facilities, found that the waves were most commonly present near interacting vortices in the NEB (Simon et al. 2018a). Specifically, they seemed to be forming to the west of prominent cyclones, and these cyclones form in former locations of prominent “bulges” of the NEB associated with an expansion episode (Fletcher et al. 2017). The Gemini 5 μm data, along with extensive 5 μm imaging from the VLT and Juno’s JIRAM instrument, demonstrated that these waves modulated cloud opacity in the 0.5–2 bar range (Adriani et al. 2018a; Fletcher et al. 2018). The wave properties are consistent with inertia-gravity waves.

Rossby waves are much larger, planetary-scale systems that are confined to propagate in the east–west direction by the Coriolis force. The best-known example of Rossby waves on Jupiter is the system of 5 μm hot spots in the southern part of the NEB, near 7°N (e.g., Ortiz et al. 1998). Both HST and Gemini components of this data set were used by Marcus et al. (2019) to investigate the properties of 5 μm hot spots, and characterize the velocities in and around them. The 5 μm hot-spot Rossby wave system is the deepest known wave in Jupiter’s atmosphere, modulating deep NH_3 concentrations as shown by microwave and millimeter wave maps from the VLA and ALMA (de Pater et al. 2016, 2019a, 2019b). This deep Rossby wave extends all the way up to the upper troposphere, as indicated by variations in the ammonia concentrations there retrieved from IRTF/TEXES data (Fletcher et al. 2016). Our

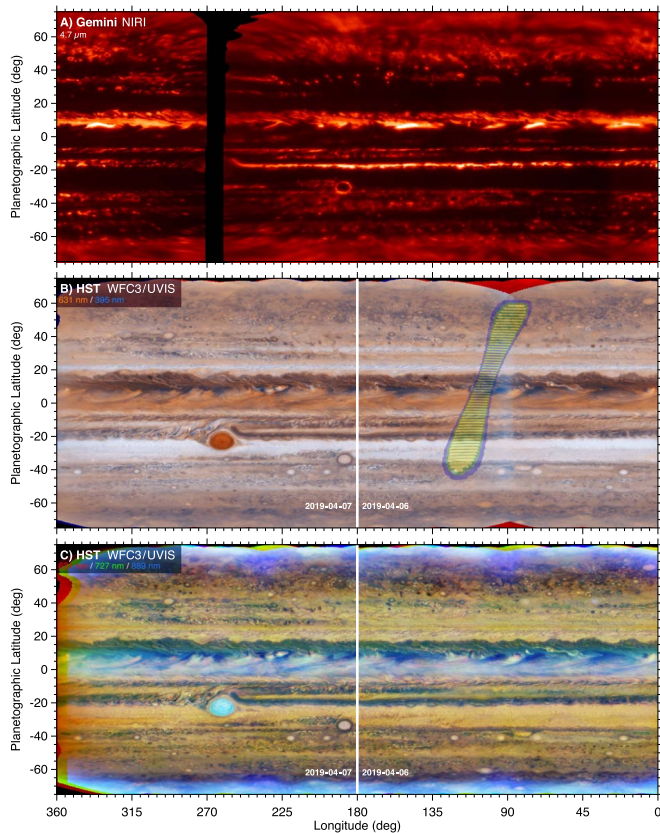


Figure 8. At the time of Juno’s 2019 cross-track orbit (see Figure 21 of Janssen et al. 2017), Gemini (panel A), the VLA (not shown), and HST (panels B and C) mapped Jupiter one hemisphere at a time over two nights. Juno MWR footprints are displayed in panel (B). Near closest approach the footprints show that MWR mapped the western half of a $5\ \mu\text{m}$ hot spot, and most likely caught one of the ammonia-rich “plumes” associated with the equatorially trapped Rossby wave (de Pater et al. 2016).

UV/visible/IR imaging data will be valuable for comparison with Juno MWR data acquired during PJ19, the cross-track mapping perijove. Juno’s scans over the NEB covered one of the $5\ \mu\text{m}$ hot spots, and most likely its adjacent “ NH_3 -plume” (de Pater et al. 2016). Figure 8 shows that not all $5\ \mu\text{m}$ hot spots are created equal; the hot spot scanned by Juno on PJ19 was not one of the infrared-brightest on that date. The relative brightness of these features is known to vary spatially as well as temporally (Ortiz et al. 1998; Orton et al. 1998).

In contrast to this deeply seated wave system, a high-altitude Rossby wave system slightly to the north near 13°N is rendered visible by its modulation of haze altitude levels (Giles et al. 2019). HST maps from 2017 April (Table 3) provided context for the upper-tropospheric wave system described by Giles et al. (2019), based on IRTF near-infrared imaging.

5.3. Convective Storms

Very large convective outbreaks on Jupiter are relatively rare, but the prevalence of lightning over the planet suggests that moist convection takes place much more frequently in smaller storms. Spacecraft imagers have detected lightning distributed all over the planet, but more concentrated in regions of cyclonic zonal wind shear (Little et al. 1999). Lightning is thought to be much more likely in the presence of mixed condensate phases (Levin et al. 1983), and water is the only liquid condensate thought to form in Jupiter’s troposphere.

Analysis of lightning flash geometry is consistent with deep flashes that occur at levels corresponding to the water cloud layer (Dyudina et al. 2002; Wong et al. 2008). Unlike Saturn, where radio emissions show that lightning is not a continuously occurring phenomenon (Dyudina et al. 2007; Sayanagi et al. 2013), Jupiter’s sferics and whistlers agree with prior imaging results, in that lightning has been detected during every Juno pass, and broadly distributed over the planet (Brown et al. 2018; Imai et al. 2018; Kolmašová et al. 2018).

Although Jupiter and Saturn differ in terms of small convective storms, they both feature large convective outbreaks (Sánchez-Lavega et al. 2017; Sánchez-Lavega et al. 2020). Giant storms break out roughly every 4–7 yr in Jupiter’s North Temperate Belt, just to the north of the fast westward jet at 23°N . One such storm erupted in late 2016, a couple months before global maps near PJ 3 allowed Jupiter’s zonal winds to be measured in 2016 December (Figure 7(C)). As in previous episodes (Sánchez-Lavega et al. 2008), the superstorms (often a pair of plumes) erupted, disturbed the cloud patterns and coloration in their vicinity, and circled the planet, finally dissipating once they had reached the tail of the disturbed region. Following this process, the westward jet’s peak speed is typically $15\ \text{m s}^{-1}$ slower than before the outbreak.

During PJ 4, Juno passed close to a somewhat smaller (but still enormous) convective storm in the SEB. This storm, a plume within a series of convective pulses that are collectively known as an SEB Outbreak, was imaged by HST and Gemini, providing context for Juno MWR measurements in its vicinity (Figure 9). In particular, a strong local depletion of ammonia in the 1–2 bar altitude range was detected by Juno MWR (Bellotti & Steffes 2017), at the location indicated by a white star in Figure 9. HST and Gemini high-resolution imaging contribute to interpretation of the results by showing that the depleted region corresponds to a dark, cloud-free region in between storm pulses. Atacama Large Millimeter/submillimeter Array (ALMA) observations of the SEB Outbreak system three months prior show that the ammonia depletion is not only present between storm plumes but in fact encircles active storm plumes (de Pater et al. 2019a). The low NH_3 concentration in this inter-storm region is consistent with the numerical model of Li & Ingersoll (2015), which also produced volatile-depleted downwelling regions in the periphery of convective storms. Radio signals detected by MWR reveal a large number of lightning flashes in the vicinity of the storm (cyan circles in Figure 9(A)). Precise location of the lightning flashes is challenged by the 20° beam size of the MWR at the lowest frequency (Brown et al. 2018), but many of the flashes may have been associated with a deep water cloud that is revealed by HST data.

5.4. The Great Red Spot

The GRS has been shrinking for over a century, and its color has also intensified over the past decade (Asay-Davis et al. 2009; Shetty & Marcus 2010; Simon et al. 2014, 2018b). The increased frequency of HST Jupiter observations during the Juno mission means that additional data are now available to characterize much shorter-term changes in the GRS, such as a 90 day oscillation in its drift rate (Reese 1971; Trigo-Rodríguez et al. 2000).

New, unexplained features in the GRS are revealed by comparing simultaneous $5\ \mu\text{m}$ and visible imaging. In

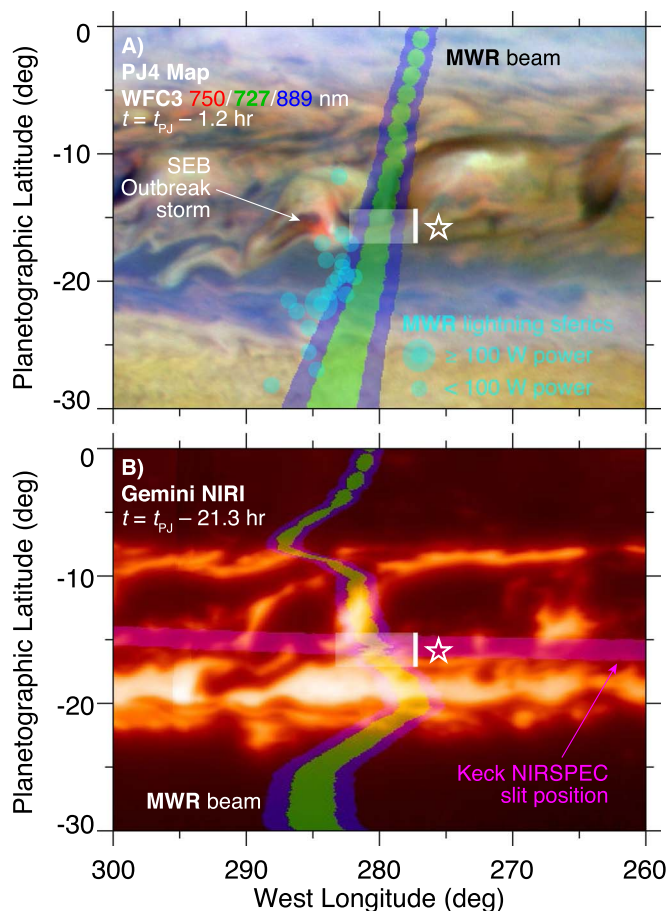


Figure 9. Juno and supporting context observations combine to reveal the most comprehensive picture yet of the convective process on Jupiter, in an example from PJ 4. Panel (A): HST multispectral imaging shows the presence of deep water clouds (in red) near the Juno MWR track (green/blue stripe). At the location marked by a white star, Juno MWR retrievals of NH_3 mixing ratio show strong ammonia depletion in the inter-storm region (Bellotti & Steffes 2017), a marker of downwelling flow consistent with dynamical models (Li & Ingersoll 2015). Lightning flashes detected by Juno MWR (Brown et al. 2018) are shown as cyan circles, each plotted at the MWR boresight pointing at the time of a lightning flash (Brown et al. 2018). Lightning is consistent with deep (water cloud level) convection in this storm. Panel (B): Gemini NIRI imaging shows regions of low cloud opacity (bright) between storm cores. The pink stripe shows Keck NIRSPEC slit position for high-resolution $5\ \mu\text{m}$ spectroscopy (Bjoraker et al. 2018a, 2018b). The footprint shows the potential of the $5\ \mu\text{m}$ spectral data to constrain the NH_3 depletion independently from Juno MWR but modeling is not yet complete.

Figure 10, holes in the clouds show up as bright features at $5\ \mu\text{m}$ and dark features at 631 nm. High-resolution $5\ \mu\text{m}$ imaging is rarely conducted, so it is not clear how rare these features are, and whether they signal a significant change in the GRS cloud layers. However, high-resolution $5\ \mu\text{m}$ images obtained with adaptive optics at the Keck Observatory did not detect these interior cloud gaps in 2006 or 2008 (de Pater et al. 2010). The Keck imaging data led to a conclusion that large anticyclones (with radius $> L_R$) like the GRS and Oval BA lack broad, continuous $5\ \mu\text{m}$ bright rings, while small anticyclones are completely encircled by $5\ \mu\text{m}$ bright rings of low cloud opacity. The Rossby deformation radius, L_R , is the characteristic length scale for geostrophic balance between buoyancy and Coriolis forces (Pedlosky 1987). The 2006 images did however show thin, incomplete $5\ \mu\text{m}$ arcs to the south of the

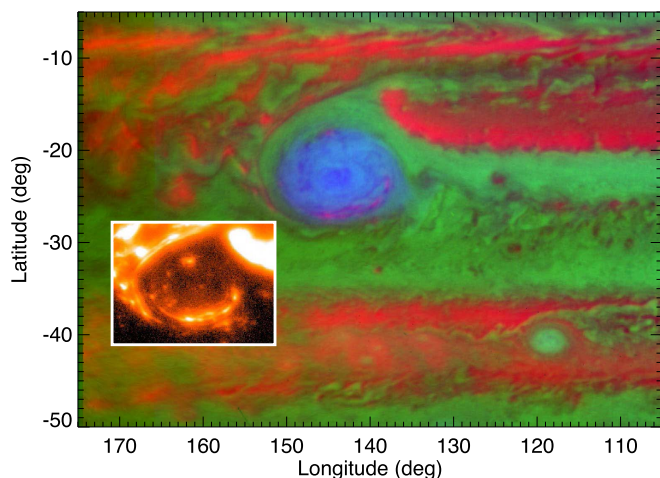


Figure 10. Nearly simultaneous Gemini and HST views of the GRS reveal the nature of dark lanes. These features are dark at visible wavelengths (green channel in composite map), and had previously been explained as either dark cloud features or areas of reduced cloud opacity (Sánchez-Lavega et al. 2018). Bright spots in the $5\ \mu\text{m}$ map (shown by itself in the inset) are only consistent with the second explanation. The enhanced GRS haze (blue channel) is uncorrelated with these areas of reduced cloud opacity.

GRS and Oval BA in 2006 but not 2008. The situation is different in the 2018 map of Figure 10, with a much more extensive southern arc composed of several concentric thin arcs and bright spots, possibly related to low-opacity regions in the northern part of the vortex that lie at similar distances from the vortex center. The main evidence for the de Pater et al. (2010, 2011) hypothesis that anticyclone circulation is fundamentally different in vortices larger or smaller than L_R , was a difference in the $5\ \mu\text{m}$ ring morphology for large and small anticyclones. In light of the evolving partial rings around the GRS and the full ring around Oval BA in Figure 8, this hypothesis may be challenged.

Sánchez-Lavega et al. (2018) described similar “dark filaments” in the JunoCam images of the GRS taken in 2017 July at PJ07. They likened the features to “dark lanes” seen in Voyager, Galileo, and Cassini imaging (e.g., Simon-Miller et al. 2001), but their radiative-transfer analysis could not distinguish between two explanations: areas of reduced cloud opacity or areas with darker cloud material. The simultaneous visible and $5\ \mu\text{m}$ imaging shown in Figure 10 clearly shows that at least during PJ 12, the dark filaments or dark lanes result from reduced cloud opacity.

5.5. Cyclonic Vortices

Within the set of Juno MWR data up to PJ 8, the largest cluster of lightning flashes was detected during PJ 6, near 45° – 50°N . Figure 11 compares the approximate location of lightning flashes with the cloud features visible to HST one Jupiter rotation later. Locations plotted are the boresight pointing positions at the time each lightning sferic was recorded by Juno’s MWR channel 1, but there is some uncertainty within the antenna beam. The 20° MWR channel 1 beam size (as projected on Jupiter) can be estimated by the

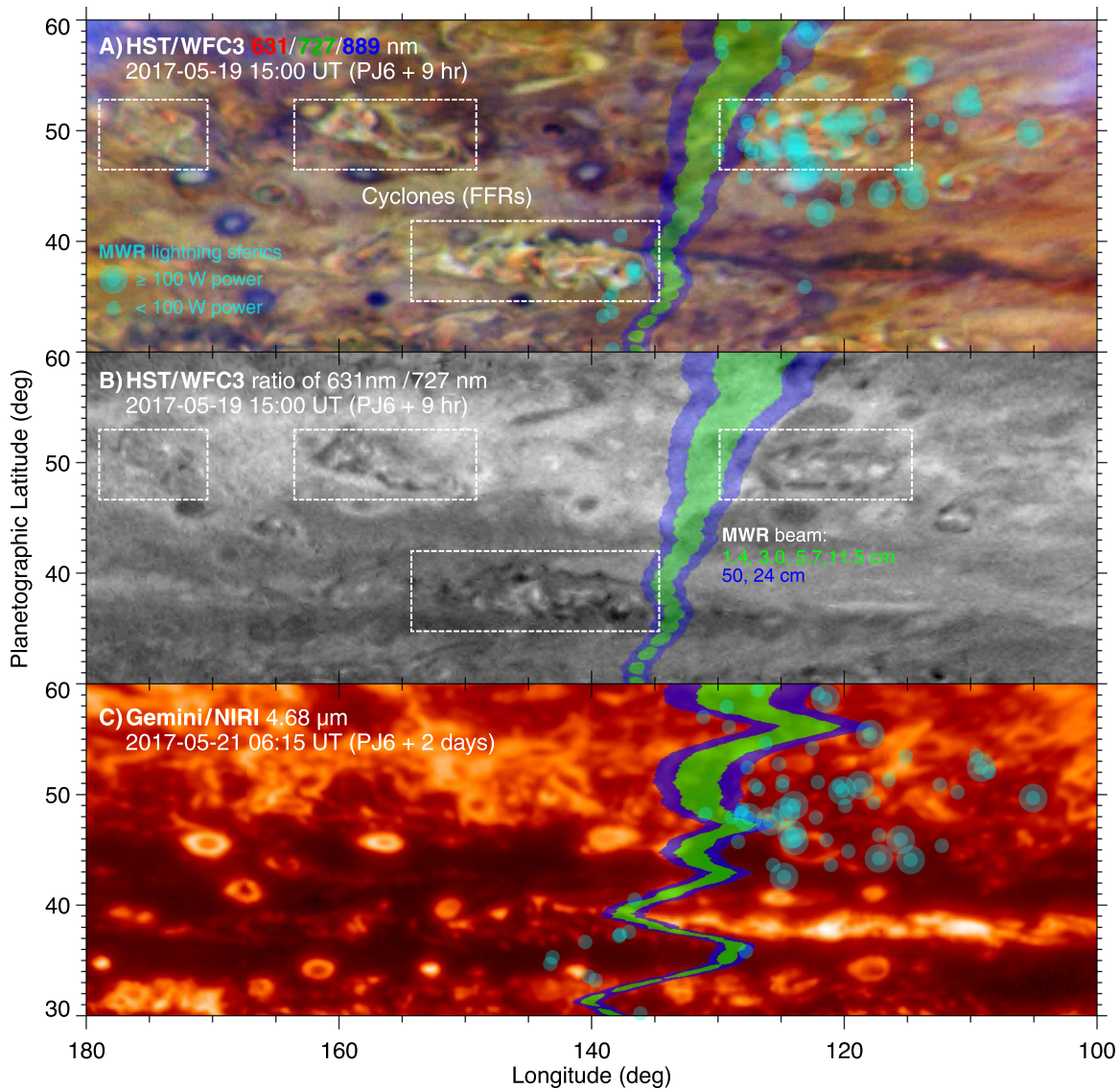


Figure 11. Cyclones (some enclosed in dashed white boxes) frequently have deep clouds ($P \geq 4$ bar), probably composed of water liquid and/or ice. During PJ 6, Juno passed close to several cyclones. Panel (A): Cloud heights are represented as color in a composite of HST data in a deep-sensing continuum filter (631 nm), and weak and strong methane bands (727 and 889 nm) that sense cloud opacity at $P < 4$ bar and $P < 0.6$ bar, respectively (see Section 5.5 for discussion of uncertainties in cloud opacity pressure levels). Panel (B): The ratio of HST 631/727 nm reflectivity is displayed as a high image brightness for deep clouds, and a low brightness for high-altitude clouds. Panel (C): Gemini 4.8 μm radiance is inversely related to cloud opacity in the 1–5 bar range. The Juno minimum-emission-angle footprint track is shown in blue and green. The Juno footprints are advected by zonal winds to account for the time delay between the spacecraft pass and the HST/Gemini imaging. The blue contour shows the variation of MWR Channel 1 beam size (half-power radius) with latitude; this is the channel most sensitive to lightning sferics. Cyan dots indicate the Channel 1 boresight position at the time of each lightning flash; the offset between the actual position of lightning flashes and the boresight pointing affects the derived effective isotropic radiating power, but this offset cannot be precisely determined. Longitudes of boresight positions have also been advected to compensate for the delay between the Juno pass and the HST/Gemini imaging. In panels (A) and (B), brightness gradients as a function of latitude have been removed (to emphasize longitudinally discrete features) by dividing the data in each latitude bin by the mean at that latitude.

width of the blue stripe in Figure 11; this shows the FWHM at the minimum emission angle sampled during each spacecraft rotation. The longitudinal width of the beam increases substantially at higher emission angles, due to perspective from the spacecraft's vantage point. Sizes of markers of lightning sferics in Figure 11 distinguish between flashes with energies above and below 100 W minimum effective isotropic radiating power. The energy estimates are lower limits because if the actual lightning flashes were located away from the boresight location, then their actual power would have been greater. Lightning locations and power estimates are taken from supplemental materials published with Brown et al. (2018).

A large number of the sferics detected in PJ 6 are associated with cyclonic vortices. Cyclonic circulation is an assumption based on the appearance of the cloud features. Only a single HST orbit was used to observe Jupiter at PJ 6, so actual velocities could not be measured to demonstrate cyclonic (counterclockwise) rotation. However, similar features (known as folded filamentary regions, or FFRs) with these types of fine-scale disorganized features, confined to a circular or elongated region, previously have been observed to rotate cyclonically. The connection between lightning, moist convection, and cyclones was discussed in Fletcher et al. (2017), following ideas that a statically stable convective inhibition layer

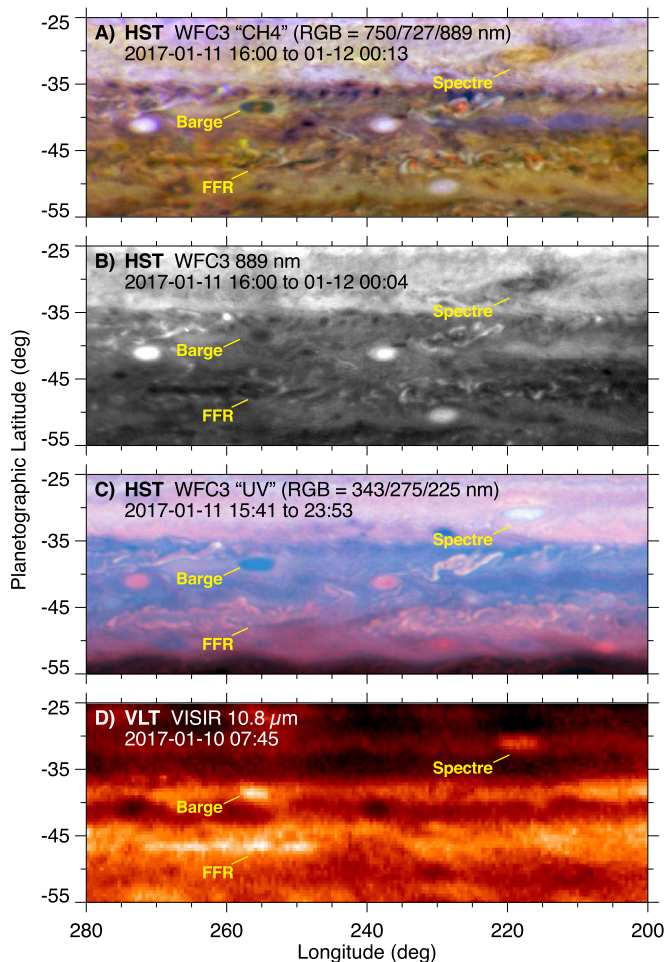


Figure 12. Types of cyclones on Jupiter have diverse appearances at wavelengths from the UV to the mid-IR. Panel (A): A composite of continuum, weak, and strong methane-band maps reveals differences in cloud heights. The deepest clouds appear only in the continuum channel (red), and must be located at $P > 4$ bar. The only clouds expected to condense this deep are composed of H_2O . The folded filamentary region (FFR) cyclone and the barge both have visible water clouds, but thick high-level clouds prevent any water clouds from being directly observed in the Spectre. Panel (B): The strong methane band is shown alone, to emphasize that all three types of cyclones have reduced upper-tropospheric haze reflectivity, relative to their surroundings. Panel (C): In the UV, there is no significant depletion of upper-tropospheric haze, indicating that the smallest particles (not sensed at 889 nm in panel B) are not destroyed or redistributed by cyclone dynamics. Panel (D): Mid-IR maps—sensitive to a combination of tropospheric temperature, ammonia, and aerosols near the 500 mbar level—show similar anomalies associated with all three cyclone types.

(Guillot 1995; Sugiyama et al. 2014; Leconte et al. 2017) is perturbed/weakened in low-pressure cyclones and regions with cyclonic zonal wind shear (Thomson & McIntyre 2016).

In the color scheme of Figure 11(A), the deepest clouds (potentially water clouds) appear red. Green and blue channels in the composite are taken in weak and strong methane bands, respectively, so that red clouds are deep, yellow clouds have significant opacity at $P < 4$ bar, and blue regions have strong upper-tropospheric haze opacity. White clouds in this scheme are thick clouds that also reach exceptionally high into the upper troposphere. In Figure 11(B), we map the continuum-to-weak CH_4 -band reflectance ratio ($I/F_{631 \text{ nm}}/I/F_{727 \text{ nm}}$), following the approaches of Banfield et al. (1998) and West et al. (2004). This ratio has high values for deep ($P > 4$ bar)

clouds and low values for higher-altitude clouds. Within the cyclonic FFRs (dashed boxes), compact deep clouds (red in Figure 11(A) and bright in Figure 11(B)) appear near the centers of the features, while thick clouds that reach high altitudes (white in Figure 11(A) and dark in Figure 11(B)) are more typically found near the outer edges. It is not obvious whether the lightning flashes reported in Brown et al. (2018) are associated with the compact deep clouds or the thick high-altitude clouds.

The presence of water clouds in these cyclonic vortices, particularly in the cyclones with strong lightning activity, is significant because lightning strongly favors mixed phase (liquid and solid) cloud particles (Levin et al. 1983). It is important to note that the pressure level of clouds that appear in continuum wavelengths (631 nm or 750 nm), but that do not appear the weak methane band (727 nm), can only be constrained by detailed radiative-transfer modeling beyond the scope of this paper. The determination that bright features in Figure 11(B) are located at $P > 4$ bar is based on the analysis of Li et al. (2006) that the 727 nm filter of Cassini/ISS reached the $\tau = 1$ level at 4 bar. However, this value is affected by viewing geometry, differences in filter bandpass between Cassini/ISS and HST/UVIS, and the presence of overlying haze and thin cloud layers. Detailed radiative-transfer analyses have been done with 727 nm and continuum maps using Galileo/SSI data, finding clouds at $P > 4$ bar in the vicinity of convective storms (Banfield et al. 1998; West et al. 2004).

Figure 12 compares three types of Jovian cyclones, in a southern-hemisphere view. FFRs near 47°S , similar to those with strong lightning activity in PJ 6, again are seen to have deep water clouds. Although we cannot directly identify the composition of these clouds based on multi-filter imaging, their location at $P > 4$ bar suggests that they are too deep to be composed of NH_4SH or NH_3 ices (Weidenschilling & Lewis 1973; Atreya & Romani 1985; Wong et al. 2015). Similarly, another type of cyclone labeled “barge” has a central water cloud. A long-lived vortex labeled “Spectre,” on the other hand, does not have detectable water clouds. But unlike the FFR and barge cyclones, the Spectre does not have regions clear of overlying cloud opacity in the $P < 4$ bar range, so any water clouds that may be present would not be detectable. Thermally, all three types of cyclones are associated with warm anomalies near the 0.5 bar level, as shown by the mid-IR map at $10.8 \mu\text{m}$. This wavelength is sensitive a combination of ammonia gas, aerosol opacity, and temperature, all consistent with downwelling flow. Haze distributions are valuable probes of the upper levels of these features. The strong methane-band (FQ889N) map shows that these cyclones are locally depleted in haze particles, but the UV images do not show a similar depletion. This difference is most likely the result of differences in the haze particle size distribution, with the larger haze particles detected near 890 nm more strongly affected by the cyclonic vortex than the small particles detected in the UV.

5.6. Polar Phenomena

Full global coverage was achieved at many of the observational epochs, enabling the polar regions to be mapped. Figure 13 gives an example of the north polar haze structure in 2017 January. “Polar” hazes extend as far south as 35°N , and as far north as 50°S . The color-composite map in Figure 13(A)

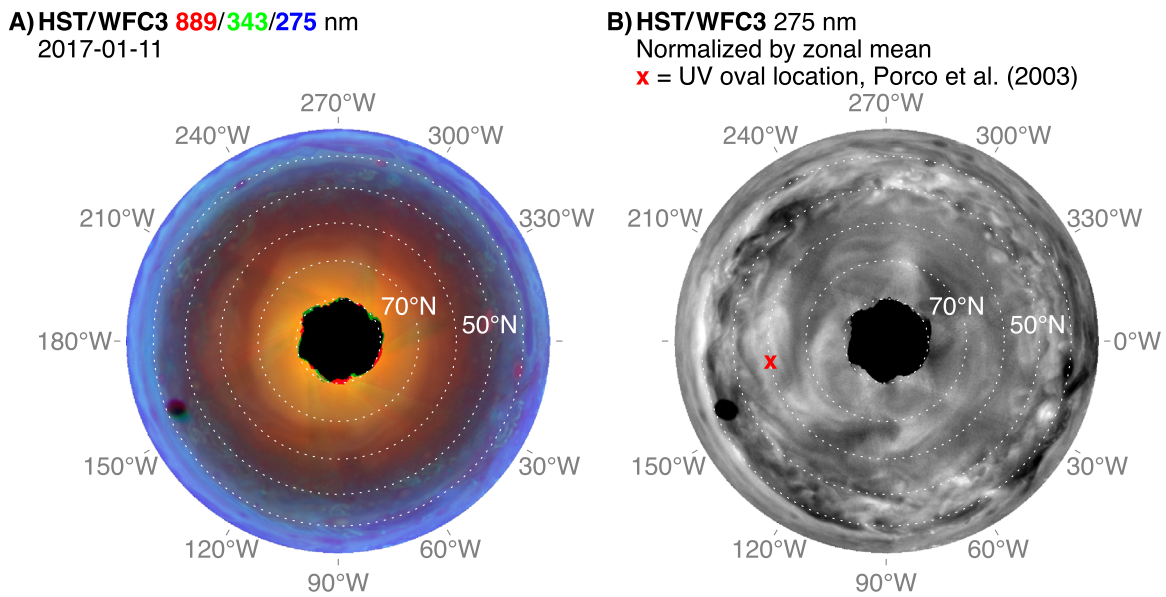


Figure 13. A north polar map shows the complex structure of polar haze “caps,” in a global mosaic composed of observations from 2017 January 11. Limb darkening has been removed from each individual frame. Panel (A): Color map combines CH_4 -band data (889 nm) in the red channel, with UV data (343 and 275 nm) in the green and blue channels. At 275 nm, the smallest haze particles, with strong UV absorption, increase in opacity near 40°N and again near 50°N . Similar boundaries are apparent at 343 nm, but the 275 nm/343 nm color ratio is different in these two concentric haze layers. The northernmost polar haze cap, with a boundary near 70°N , is characterized by strong reflectivity at 889 nm and 343 nm, but is hardly discernible at 275 nm or 225 nm (not shown). Each concentric polar haze cap has wave-like structures around its boundary, and the innermost cap near 70°N is suggestive of a somewhat irregular decahedral or hendecahedral pattern. Panel (B): The 275 nm mosaic has been normalized by the zonal mean at each latitude, revealing longitudinal variation in reflectivity. The dark UV oval described in Porco et al. (2003) and West et al. (2004) is absent at this epoch. The shadow of Ganymede can be seen in the mosaics near 155°W and 45°N .

demonstrates significant changes in haze properties every $\sim 10^\circ$ of latitude in the wavelengths shown, between 40°N and 80°N . Detailed radiative-transfer modeling beyond the scope of this paper is needed to understand what causes these meridional changes in haze properties, but multiple effects are probably at work. Each filter has different vertical sensitivity, so vertical layering of polar hazes may explain some of the meridional variation. Hazes are bright in the near-IR CH_4 band, but absorbing at UV wavelengths, so some of the reflectivity variation is linked to composition. Particle size effects are also significant across such a wide range of wavelengths. Much of the polar stratospheric haze is thought to be generated by methane photolysis, driven by solar UV (West et al. 1986). Differences in stratospheric composition at high latitudes have been measured by Cassini CIRS (Nixon et al. 2007). But auroral chemistry may also contribute to the haze cap north of 70°N , within which a UV-dark oval has been reported at some epochs (Porco et al. 2003; West et al. 2004).

6. Conclusions

Our imaging context from HST and Gemini give the highest-resolution global views of Jupiter at visible and $5\ \mu\text{m}$ wavelengths during the Juno mission (similar $5\ \mu\text{m}$ resolution is achieved at some epochs with VLT/VISIR, Fletcher et al. 2018). This contextual information is helpful for interpreting spatial variation in ammonia mixing ratios derived from Juno MWR measurements. In one specific example, the imaging context on PJ 4 (Figure 9) reveals that Juno’s sub-spacecraft track passed between convective storm cores in the SEB, where depleted ammonia concentration detected by the Juno MWR (Bellotti & Steffes 2017) indicates strong downwelling. Accurate placement of the Juno track with respect to the storm allows quantitative comparison with numerical models of

convection such as Li & Ingersoll (2015). In addition to studying the convective process, the data set is well-suited to studies of jets, waves, vortices, hazes, clouds, and circulation.

The 53 day cadence driven by the Juno orbital period synchronizes a worldwide coordinated observational effort across a wide range of the spectrum, from UV data shown here and in Grodent et al. (2018), to data in the millimeter and radio regime (de Pater et al. 2019a, 2019b). Our synchronized observations of the GRS (Figure 10) are able to distinguish between explanations of dark features within this iconic storm system (Sánchez-Lavega et al. 2018), showing that they are regions of reduced cloud opacity rather than regions with darker cloud particles.

A strong emphasis has been placed on providing HLSPs from the HST and Gemini data sets into the MAST archive.¹⁹ The combined data set should support a wide range of unanticipated science investigations, enabled by its regular sampling at 53 day intervals over the multi-year duration of the Juno mission.

Based on observations obtained with NIRI at the Gemini Observatory, which is operated by the Association of Universities for Research in Astronomy, Inc. (AURA), under a cooperative agreement with the NSF on behalf of the international Gemini partnership: the National Science Foundation (United States), National Research Council (Canada), CONICYT (Chile), Ministerio de Ciencia, Tecnología e Innovación Productiva (Argentina), Ministério da Ciência, Tecnologia e Inovação (Brazil), and Korea Astronomy and Space Science Institute (Republic of Korea); on observations

¹⁹ WFC3 HLSPs are available in doi:10.17909/T94T1H, and OPAL HLSPs are available in Simon (2015).

made with WFC3 on the NASA/ESA Hubble Space Telescope, obtained at the Space Telescope Science Institute, which is operated by AURA under NASA contract NAS 5-26555; on observations obtained with VLT/VISIR at the European Organisation for Astronomical Research in the Southern Hemisphere (under ESO programme 098.C-0681D).

This publication does not include data from the NASA Juno mission, other than MWR boresight pointings (at times of lightning sferic detections) that are publicly available as part of Brown et al. (2018), and timing and pointing data available from the Mission Juno public website (<https://missionjuno.swri.edu>).

Team members' contributions were supported by the Space Telescope Science Institute (for program numbers listed in Table 3), which is operated by AURA under NASA contract NAS 5-26555; by NASA under Cooperative Agreement 80NSSC19M0189, grant NNX16AP12H issued through the NASA Earth and Space Science Fellowship program, grants NNX14AJ43G and 80NSSC18K1001 issued through the Planetary Astronomy program, grant NNX16AP12H issued through the Earth and Space Science Fellowship program, and grant NNX15AJ41G issued through the Solar System Observations program; by the Gemini Observatory, which is operated

by AURA on behalf of the international Gemini partnership; by NASA through the Juno Project; by NASA to the Jet Propulsion Laboratory, California Institute of Technology; by a Royal Society Research Fellowship; and by European Research Council Consolidator grant No. 723890 issued by the European Union's Horizon 2020 research and innovation programme.

This work was enabled by the location of the Gemini North telescope within the Maunakea Science Reserve, adjacent to the summit of Maunakea. We are grateful for the privilege of observing Ka'āwela (Jupiter) from a place that is unique in both its astronomical quality and its cultural significance.

Appendix Additional Periodograms

Figure 6 presents periodogram analyses for two sets of data, as discussed in Section 5.1. Table 6 lists several additional sets that were analyzed for periodicity, all of which are shown in this Appendix. For each periodogram shown in Figures 14–20, the caption gives the subset of zonal wind measurements (Table 6) used in the analysis.

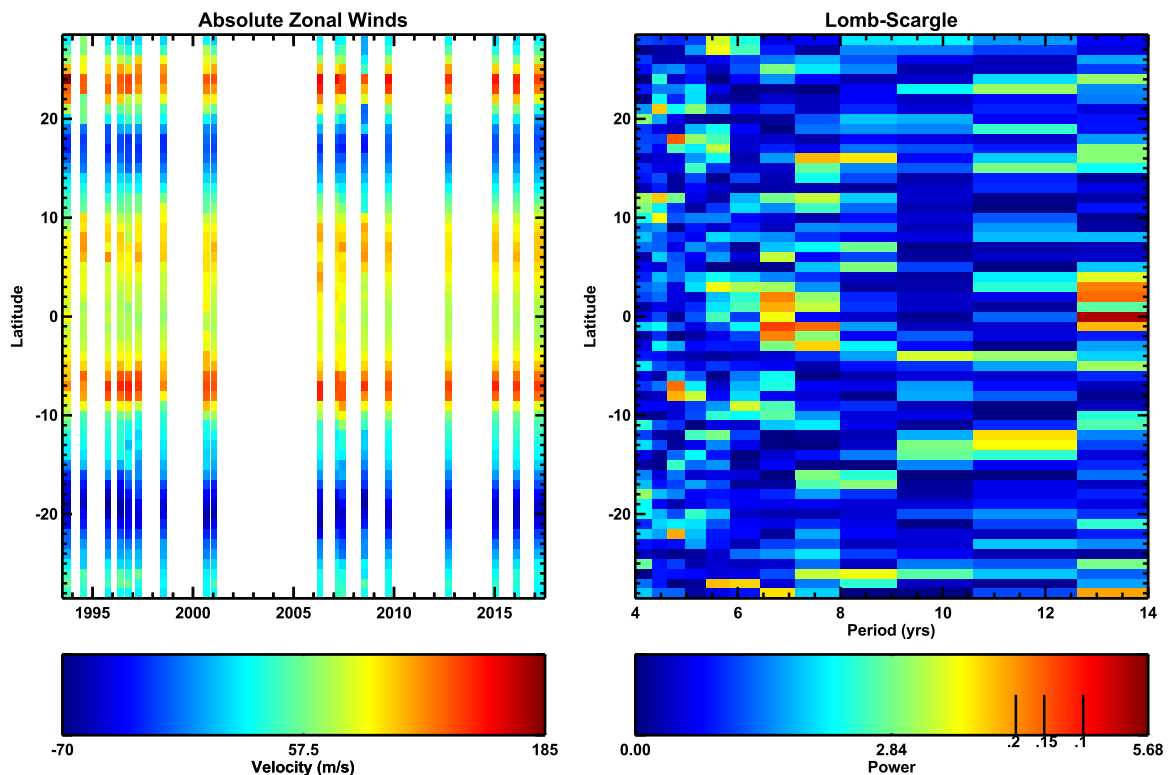


Figure 14. Zonal wind and periodogram data and colors as described in Figure 6, for the “Tollefson et al. (2017)” set in Table 6.

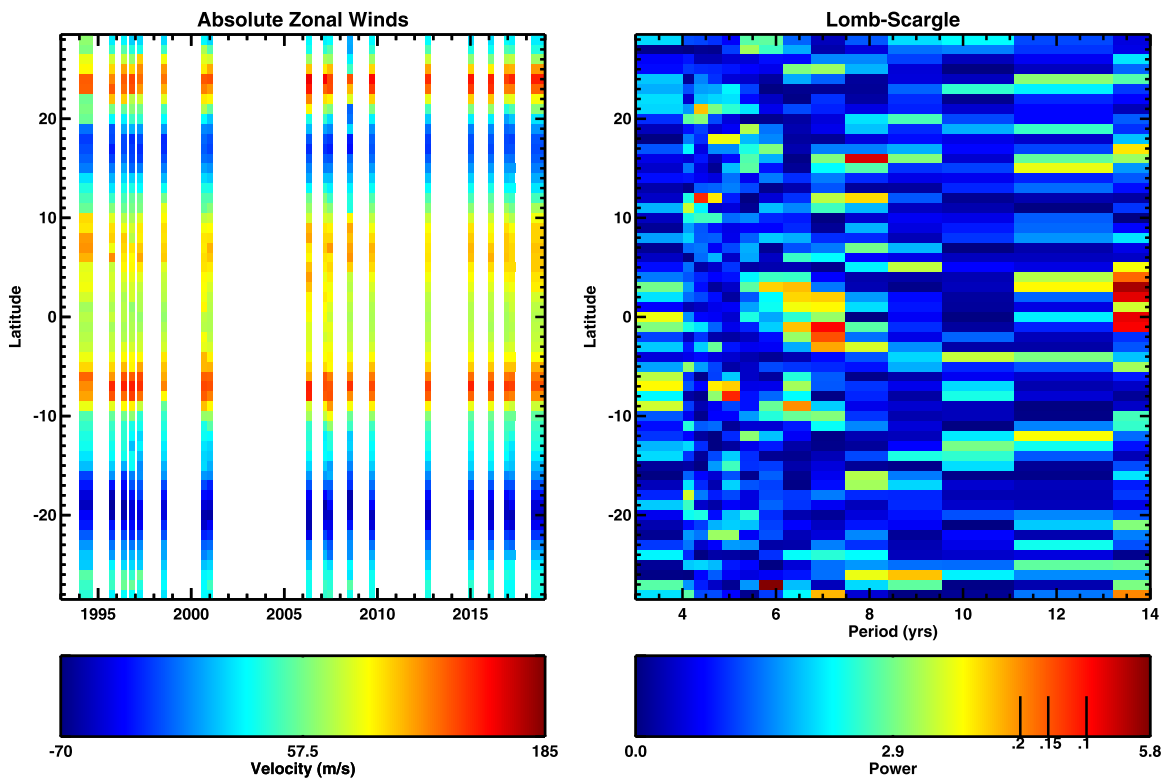


Figure 15. Zonal wind and periodogram data and colors as described in Figure 6, for the “Subset 2018” set in Table 6.

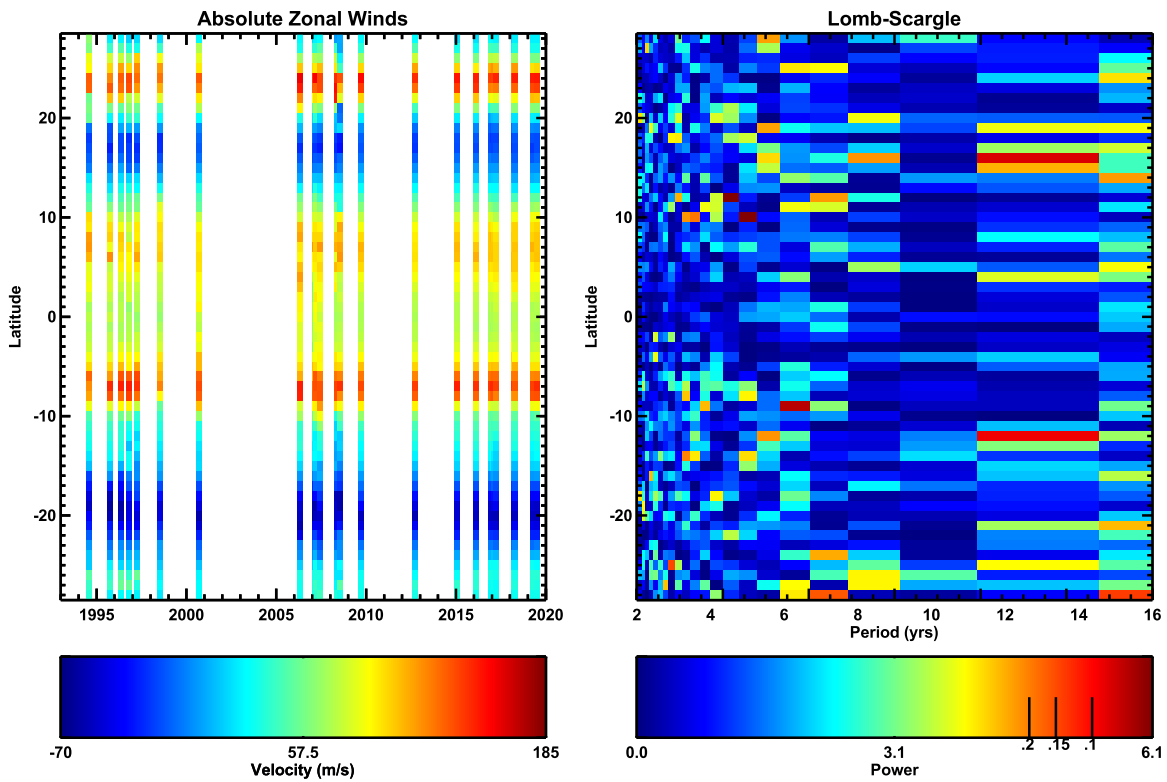


Figure 16. Zonal wind and periodogram data and colors as described in Figure 6, for the “HST only” set in Table 6.

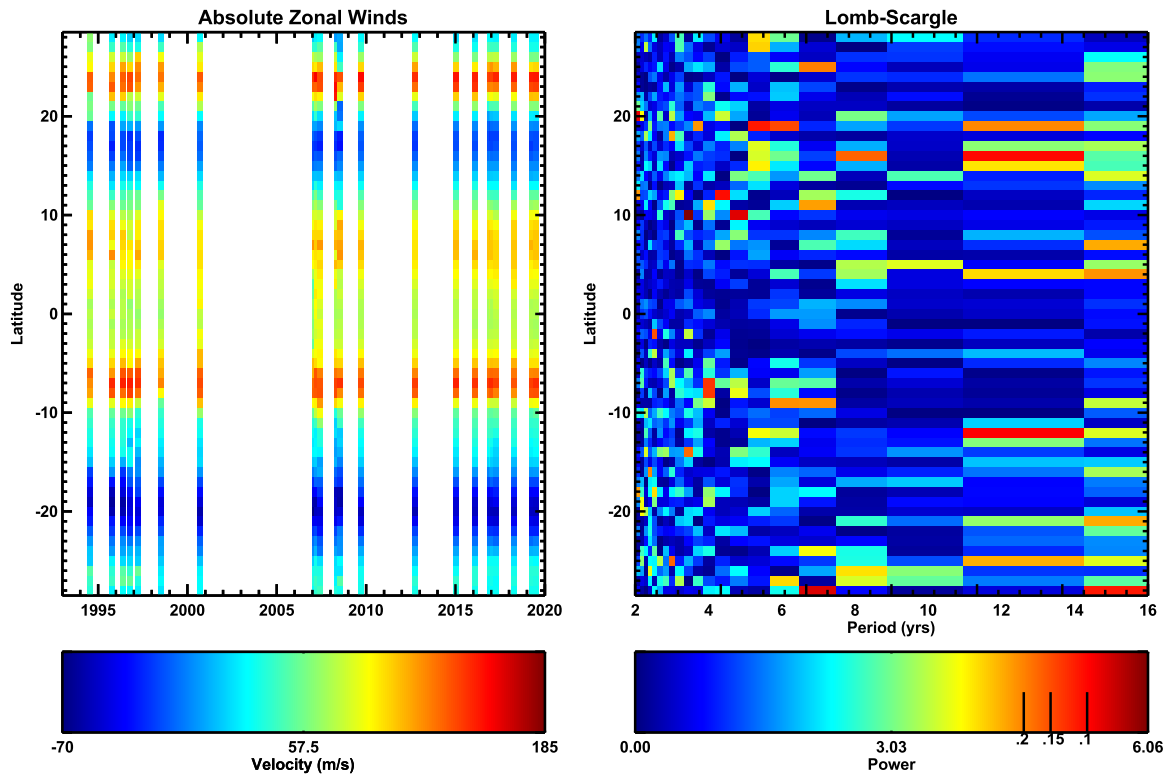


Figure 17. Zonal wind and periodogram data and colors as described in Figure 6, for the “WFPC2 + WFC3” set in Table 6.

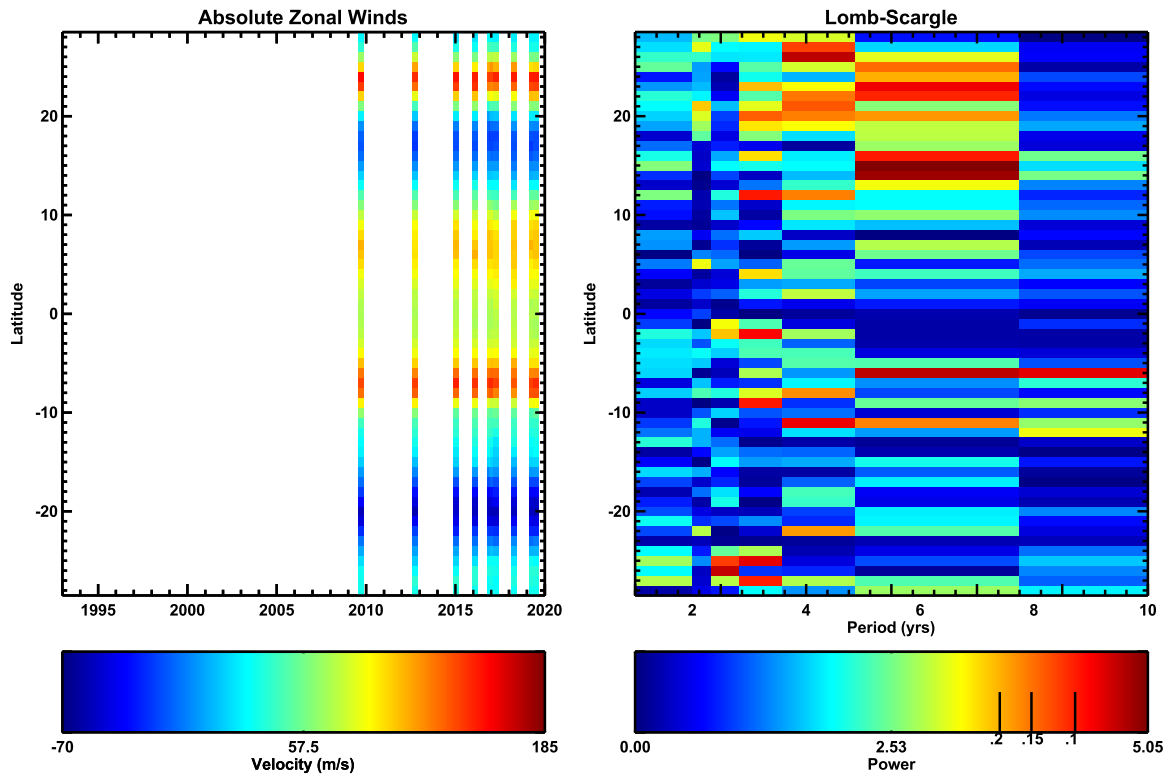


Figure 18. Zonal wind and periodogram data and colors as described in Figure 6, for the “WFC3 only” set in Table 6.

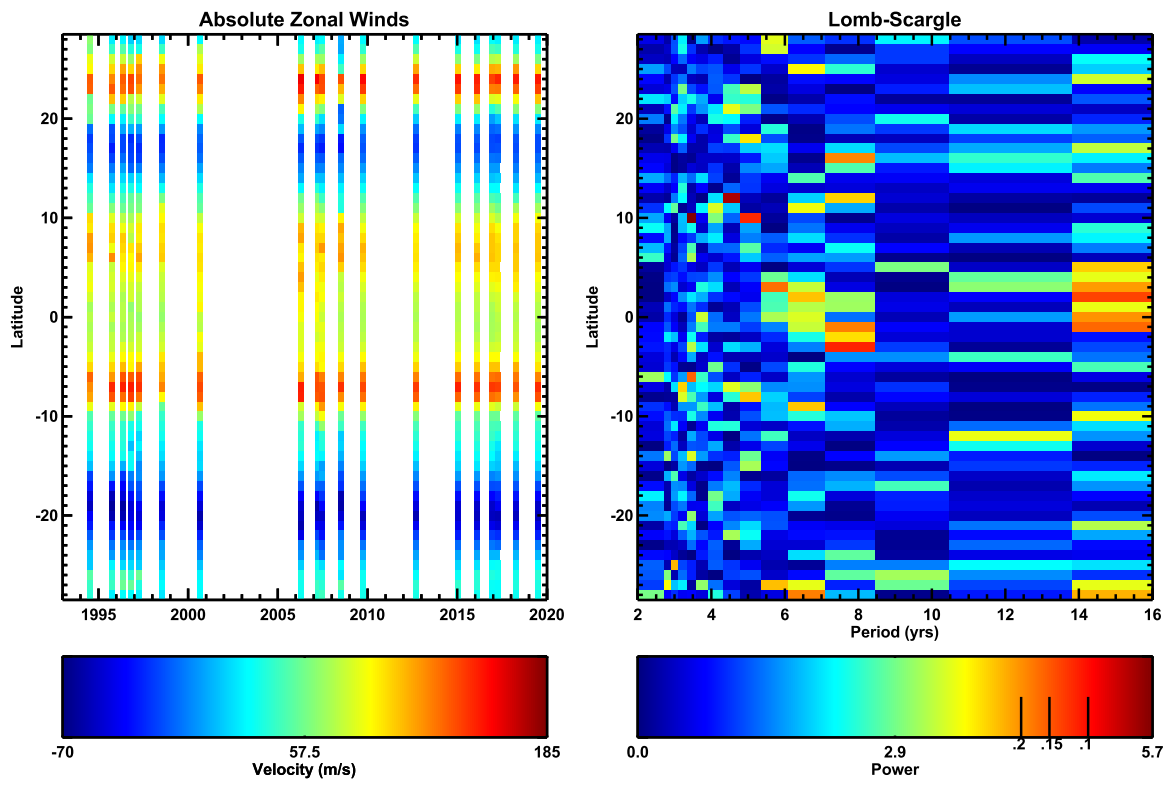


Figure 19. Zonal wind and periodogram data and colors as described in Figure 6, for the “WFC3 only (filtered)” set in Table 6.

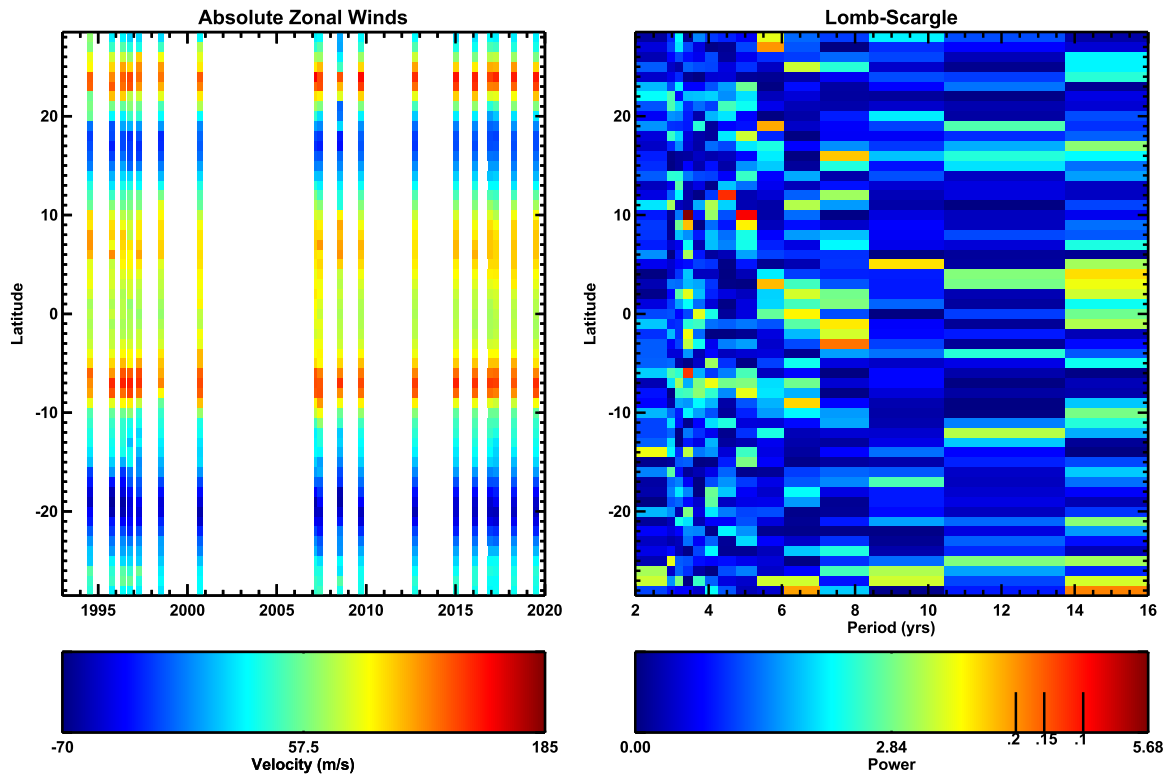


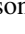






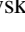






Figure 20. Zonal wind and periodogram data and colors as described in Figure 6, for the “WFPC2 + WFC3 (filtered)” set in Table 6.

ORCID iDs

Michael H. Wong  <https://orcid.org/0000-0003-2804-5086>
 Amy A. Simon  <https://orcid.org/0000-0003-4641-6186>
 Joshua W. Tollefson  <https://orcid.org/0000-0003-2344-634X>
 Imke de Pater  <https://orcid.org/0000-0002-4278-3168>
 Megan N. Barnett  <https://orcid.org/0000-0003-4804-577X>
 Andrew I. Hsu  <https://orcid.org/0000-0002-6190-9336>
 Andrew W. Stephens  <https://orcid.org/0000-0002-4434-2307>
 Glenn S. Orton  <https://orcid.org/0000-0001-7871-2823>
 Scott W. Fleming  <https://orcid.org/0000-0003-0556-027X>
 William Januszewski  <https://orcid.org/0000-0002-3545-1157>
 Anthony Roman  <https://orcid.org/0000-0001-5040-8520>
 Gordon L. Bjoraker  <https://orcid.org/0000-0002-9679-4153>
 Alberto Adriani  <https://orcid.org/0000-0003-4998-8008>
 Leigh N. Fletcher  <https://orcid.org/0000-0001-5834-9588>

References

- Achterberg, R. K., Conrath, B. J., & Gierasch, P. J. 2006, *Icar*, **182**, 169
 Adriani, A., Moriconi, M. L., Altieri, F., et al. 2018a, *AJ*, **156**, 246
 Adriani, A., Mura, A., Orton, G., et al. 2018b, *Natur*, **555**, 216
 Antuñano, A., Fletcher, L. N., Orton, G. S., et al. 2018, *GeoRL*, **45**, 10987
 Asay-Davis, X. S., Marcus, P. S., Wong, M. H., & de Pater, I. 2009, *Icar*, **203**, 164
 Asay-Davis, X. S., Marcus, P. S., Wong, M. H., & de Pater, I. 2011, *Icar*, **211**, 1215
 Atkinson, D. H., Pollack, J. B., & Seiff, A. 1998, *JGR*, **103**, 22911
 Atreya, S. K., & Romani, P. N. 1985, in *Planetary Meteorology*, ed. G. E. Hunt (Cambridge: Cambridge Univ. Press), 17
 Baggett, S., Gosmeyer, C., & Noeske, K. 2015, WFC3/UVIS Charge Transfer Efficiency 2009–2015, Tech. Rep. WFC3 ISR 2015-03 (Baltimore, MD: STScI)
 Banfield, D., Gierasch, P. J., Bell, M., et al. 1998, *Icar*, **135**, 230
 Beebe, R. F., Ingersoll, A. P., Hunt, G. E., Mitchell, J. L., & Muller, J.-P. 1980, *GeoRL*, **7**, 1
 Bellotti, A., & Steffes, P. G. 2017, AAS Meeting Abstract, **49**, 118.03
 Bjoraker, G., Wong, M., de Pater, I., et al. 2018a, AAS Meeting Abstract, **50**, 500.03
 Bjoraker, G. L., Larson, H. P., & Kunde, V. G. 1986, *ApJ*, **311**, 1058
 Bjoraker, G. L., Wong, M. H., de Pater, I., Hewagama, T., Ádámkóvics, M., & Orton, G. S. 2018b, *AJ*, **156**, 101
 Bolton, S. J., Lunine, J., Stevenson, D., et al. 2017, *SSRv*, **213**, 5
 Braude, A. S., Irwin, P., Orton, G., & Fletcher, L. 2020, *Icar*, **338**, 113589
 Brown, S., Janssen, M., Adumitroaie, V., et al. 2018, *Natur*, **558**, 87
 Carlson, R. W., Weissman, P. R., Smythe, W. D., & Mahoney, J. C. 1992, *SSRv*, **60**, 457
 Choi, D. S., Banfield, D., Gierasch, P., & Showman, A. P. 2007, *Icar*, **188**, 35
 Christou, J., Neichel, B., Rigaut, F., et al. 2010, *Proc. SPIE*, **7736**, 77361R
 Colina, L., Bohlin, R. C., & Castelli, F. 1996, *ApJ*, **112**, 307
 Dahl, E., Chanover, N. J., Voelz, D., et al. 2018, AAS Meeting, **50**, 214.17
 Danielsson, P. E., & Seger, O. 1990, in *Machine vision for Three-dimensional scenes*, ed. F. Herbert (New York: Academic), 347
 de Pater, I., Sault, R. J., Butler, B., DeBoer, D., & Wong, M. H. 2016, *Sci*, **352**, 1198
 de Pater, I., Sault, R. J., Moeckel, C., et al. 2019a, *AJ*, **158**, 139
 de Pater, I., Sault, R. J., Wong, M. H., et al. 2019b, *Icar*, **322**, 168
 de Pater, I., Wong, M. H., de Kleer, K., et al. 2011, *Icar*, **213**, 559
 de Pater, I., Wong, M. H., Marcus, P., et al. 2010, *Icar*, **210**, 742
 Deustua, S. E., Mack, J., Bajaj, V., & Khandrika, H. 2017, WFC3/UVIS Updated 2017 Chip-Dependent Inverse Sensitivity Values, Tech. Rep. WFC3 ISR 2017-14 (Baltimore, MD: STScI)
 Deustua, S. E., Mack, J., Bowers, A. S., et al. 2016, UVIS 2.0 Chip-dependent Inverse Sensitivity Values, Tech. Rep. WFC3 ISR 2016-03 (Baltimore, MD: STScI)
 Dressel, L. 2019, *Wide Field Camera 3 Instrument Handbook v11.0* (Baltimore, MD: STScI)
 Dyudina, U. A., Ingersoll, A. P., Ewald, S. P., et al. 2007, *Icar*, **190**, 545
 Dyudina, U. A., Ingersoll, A. P., Vasavada, A. R., Ewald, S. P. & the Galileo SSI Team 2002, *Icar*, **160**, 336
 Fletcher, L. N., Greathouse, T. K., Orton, G. S., et al. 2016, *Icar*, **278**, 128
 Fletcher, L. N., Melin, H., Adriani, A., et al. 2018, *AJ*, **156**, 67
 Fletcher, L. N., Orton, G. S., Sinclair, J. A., et al. 2017, *GeoRL*, **44**, 7140
 Fountain, J. W., Coffeen, D. L., Doose, L. R., et al. 1974, *Sci*, **184**, 1279
 Gierasch, P. J., Conrath, B. J., & Magalhães, J. A. 1986, *Icar*, **67**, 456
 Gierasch, P. J., Ingersoll, A. P., Banfield, D., et al. 2000, *Natur*, **403**, 628
 Giles, R. S., Orton, G. S., Stephens, A. W., et al. 2019, *GeoRL*, **46**, 1232
 Grodent, D., Bonfond, B., Yao, Z., et al. 2018, *JGRA*, **123**, 3299
 Guillot, T. 1995, *Sci*, **269**, 1697
 Harrington, J., Dowling, T. E., & Baron, R. L. 1996, *Icar*, **124**, 22
 Hodapp, K. W., Jensen, J. B., Irwin, E. M., et al. 2003, *PASP*, **115**, 1388
 Hueso, R., Legarreta, J., García-Melendo, E., Sánchez-Lavega, A., & Pérez-Hoyos, S. 2009, *Icar*, **203**, 499
 Hueso, R., Sánchez-Lavega, A., Iñurrigarro, P., et al. 2017, *GeoRL*, **44**, 4669
 Imai, M., Santolík, O., Brown, S. T., et al. 2018, *GeoRL*, **45**, 7268
 Janssen, M. A., Oswald, J. E., Brown, S. T., et al. 2017, *SSRv*, **213**, 139
 Johnson, P. E., Morales-Juberías, R., Simon, A., et al. 2018, *P&SS*, **155**, 2
 Karkoschka, E. 1998, *Icar*, **133**, 134
 Kolmašová, I., Imai, M., Santolík, O., et al. 2018, *NatAs*, **2**, 544
 Kozhurina-Platais, V. 2014, *Astrometric Correction for WFC3/UVIS Filter-Dependent Component of Distortion*, Tech. Rep. WFC3 ISR 2014-12 (Baltimore, MD: STScI)
 Lecote, J., Selsis, F., Hersant, F., & Guillot, T. 2017, *A&A*, **598**, A98
 Levin, Z., Borucki, W. J., & Toon, O. B. 1983, *Icar*, **56**, 80
 Li, C., Ingersoll, A., Janssen, M., et al. 2017, *GeoRL*, **44**, 5317
 Li, C., & Ingersoll, A. P. 2015, *NatGe*, **8**, 398
 Li, L., Ingersoll, A. P., Vasavada, A. R., et al. 2006, *JGRE*, **111**, E04004
 Lii, P. S., Wong, M. H., & de Pater, I. 2010, *Icar*, **209**, 591
 Limaye, S. S. 1986, *Icar*, **65**, 335
 Little, B., Anger, C. D., Ingersoll, A. P., et al. 1999, *Icar*, **142**, 306
 Lupie, O., Hanley, C., & Nelan, J. 2000, *Wide Field Camera #3 Filter Selection Process - Part II: Compendium of Community Input*, Tech. Rep. WFC3 ISR 2000-08 (Baltimore, MD: STScI)
 Mack, J., Dahlen, T., Sabbi, E., & Bowers, A. S. 2016, *UVIS 2.0: Chip-Dependent Flats*, Tech. Rep. WFC3 ISR 2016-04 (Baltimore, MD: STScI)
 Marcus, P. S., Tollefson, J., Wong, M. H., & de Pater, I. 2019, *Icar*, **324**, 198
 Martlin, Kozhurina-Platais, V., McKay, M., & Sabbi, E. 2018, *Updates to the WFC3/UVIS Filter-Dependent and Geometric Distortions*, Tech. Rep. WFC3 ISR 2018-10 (Baltimore, MD: STScI)
 Miller, E. A., Klein, G., Juergens, D. W., et al. 1996, *Proc. SPIE*, **2803**, 206
 Mitchell, J. L., Beebe, R. F., Ingersoll, A. P., & Garneau, G. W. 1981, *JGR*, **86**, 8751
 Nixon, C. A., Achterberg, R. K., Conrath, B. J., et al. 2007, *Icar*, **188**, 47
 Ortiz, J. L., Orton, G. S., Friedson, A. J., et al. 1998, *JGR*, **103**, 23051
 Orton, G. S., Fisher, B. M., Baines, K. H., et al. 1998, *JGR*, **103**, 22791
 Osten, R. 2019, *STScI Newsletter*, **36**, 1, <http://www.stsci.edu/contents/newsletters/2019-volume-36-issue-01/hst-stsci-update>
 Osten, R., & Brown, T. 2018, *STScI Newsletter*, **35**, 3, <http://www.stsci.edu/contents/newsletters/2018-volume-35-issue-03/hubbles-gyros-cause-a-stir>
 Pedlosky, J. 1987, *Geophysical Fluid Dynamics* (New York: Springer)
 Porco, C. C., West, R. A., McEwen, A., et al. 2003, *Sci*, **299**, 1541
 Rector, T. A., Levay, Z. G., Frattare, L. M., English, J., & Pu'uhou-Pummill, K. 2007, *AJ*, **133**, 598
 Reese, E. J. 1971, *Icar*, **14**, 343
 Ryan, R. E., Jr., Deustua, S., Anderson, J., et al. 2016, *The Updated Calibration Pipeline for WFC3/UVIS: A Reference Guide to Calwf3 3.3*, Tech. Rep. WFC3 ISR 2016-01 (Baltimore, MD: STScI)
 Salyk, C., Ingersoll, A. P., Lorre, J., Vasavada, A., & Del Genio, A. D. 2006, *Icar*, **185**, 430
 Sánchez-Lavega, A., García-Melendo, E., & Legarreta, J. 2020, *NatAs*, **4**, 180
 Sánchez-Lavega, A., Hueso, R., Eichstädt, G., et al. 2018, *AJ*, **156**, 9
 Sánchez-Lavega, A., Orton, G. S., Hueso, R., et al. 2008, *Natur*, **451**, 437
 Sánchez-Lavega, A., Rogers, J. H., Orton, G. S., et al. 2017, *GeoRL*, **44**, 4679
 Sayanagi, K. M., Dyudina, U. A., Ewald, S. P., et al. 2013, *Icar*, **223**, 460
 Shetty, S., & Marcus, P. S. 2010, *Icar*, **210**, 182
 Simon, A. 2015, *Outer Planet Atmospheres Legacy (“OPAL”)*, MAST, doi:10.17909/T9G593
 Simon, A. A. 1999, *Icar*, **141**, 29
 Simon, A. A., Hueso, R., Iñurrigarro, P., et al. 2018a, *AJ*, **156**, 79

- Simon, A. A., Tabataba-Vakili, F., Cosentino, R., et al. 2018b, *AJ*, **155**, 151
- Simon, A. A., Wong, M. H., & Orton, G. S. 2015, *ApJ*, **812**, 55
- Simon, A. A., Wong, M. H., Rogers, J. H., et al. 2014, *ApJL*, **797**, L31
- Simon-Miller, A. A., Banfield, D., & Gierasch, P. J. 2001, *Icar*, **154**, 459
- Simon-Miller, A. A., & Gierasch, P. J. 2010, *Icar*, **210**, 258
- Simon-Miller, A. A., Poston, B. W., Orton, G. S., & Fisher, B. 2007, *Icar*, **186**, 192
- Simon-Miller, A. A., Rogers, J. H., Gierasch, P. J., et al. 2012, *Icar*, **218**, 817
- Sindoni, G., Grassi, D., Adriani, A., et al. 2017, *GeoRL*, **44**, 4660
- Smith, B. A., Soderblom, L. A., Johnson, T. V., et al. 1979, *Sci*, **204**, 951
- Sugiyama, K., Nakajima, K., Odaka, M., Kuramoto, K., & Hayashi, Y.-Y. 2014, *Icar*, **229**, 71
- Thomson, S. I., & McIntyre, M. E. 2016, *JAtS*, **73**, 1119
- Tokunaga, A. T. 2000, in *Allen's Astrophysical Quantities*, ed. A. N. Cox (4th ed.; New York: Springer), 143
- Tollefson, J., Wong, M. H., Pater, I. d., et al. 2017, *Icar*, **296**, 163
- Trigo-Rodríguez, J. M., Sánchez-Lavega, A., Gómez, J. M., et al. 2000, *P&SS*, **48**, 331
- Trujillo, C., Ball, J., Boccas, M., et al. 2013, in *Proc. Third Adaptive Optics for Extremely Large Telescopes Conf.*, ed. S. Esposito & L. Fini (Singapore: World Scientific), 51
- van Dokkum, P. G. 2001, *PASP*, **113**, 1420
- Weidenschilling, S. J., & Lewis, J. S. 1973, *Icar*, **20**, 465
- West, R. A., Baines, K. H., Friedson, A. J., et al. 2004, in *Jupiter: The Planet, Satellites and Magnetosphere*, ed. F. Bagenal et al. (Cambridge: Cambridge Univ. Press), 79
- West, R. A., Strobel, D. F., & Tomasko, M. G. 1986, *Icar*, **65**, 161
- Westphal, J. A. 1969, *ApJL*, **157**, L63
- Wong, M. H. 2010, *Amplitude of Fringing in WFC3/UVIS Narrowband Red Filters*, Tech. Rep. WFC3 ISR 2010-04 (Baltimore, MD: STScI)
- Wong, M. H. 2011, in *Proc. 2010 STScI Calibration Workshop*, ed. S. Deustua & C. Oliveira (Baltimore, MD: STScI), 189
- Wong, M. H., Atreya, S. K., Kuhn, W. R., Romani, P. N., & Mihalka, K. M. 2015, *Icar*, **245**, 273
- Wong, M. H., Lunine, J., Atreya, S. K., et al. 2008, *RvMG*, **68**, 219
- Wong, M. H., Tollefson, J., Hsu, A. I., et al. 2018, *AJ*, **155**, 117